Analysis of the characteristics and mechanisms of the Pacific Decadal Oscillation in a suite of coupled models from the Geophysical Fluid Dynamics Laboratory

Liping Zhang[1& 2] and Thomas L. Delworth[2],

[1]Atmospheric and Oceanic Science
Princeton University
New Jersey, U.S.

[2]NOAA/Geophysical Fluid Dynamics Laboratory, Princeton
New Jersey, U.S.

Revised to *Journal of Climate*
June, 2015

Corresponding author address: Liping Zhang, NOAA/Geophysical Fluid Dynamics Laboratory, 201 Forrestal Rd., Princeton, NJ 08540. E-mail: Liping.Zhang@noaa.gov

Abstract

North Pacific decadal oceanic and atmospheric variability is examined in a suite of coupled climate models developed at the Geophysical Fluid Dynamics Laboratory (GFDL). The models have ocean horizontal resolutions ranging from 1^o to 0.1^o, and atmospheric horizontal resolutions ranging from 200km to 50km. In all simulations the dominant pattern of decadal-scale sea surface temperature (SST) variability over the North Pacific is similar to the observed Pacific Decadal Oscillation (PDO). Simulated SST anomalies in the Kuroshio Oyashio Extension (KOE) region exhibit a significant spectral peak at approximately 20 years.

We use sensitivity experiments to show that: (i) the simulated PDO mechanism involves extratropical air-sea interaction and oceanic Rossby wave propagation, (ii) the oscillation can exist independent of interactions with the Tropics, but that such interactions can enhance the PDO, and (iii) ocean to atmosphere feedback in the extratropics is critical for establishing the approximately 20-year timescale of the PDO. The spatial pattern of the PDO can be generated from atmospheric variability that occurs independently of ocean-atmosphere feedback, but the existence of a spectral peak depends on active air-sea coupling. The specific interdecadal timescale is strongly influenced by the propagation speed of oceanic Rossby waves in the subtropical and subpolar gyres, as they provide a delayed feedback to the atmosphere.

The simulated PDO has a realistic association with precipitation variations over North America, with a warm phase of the PDO generally associated with positive precipitation anomalies over regions of the western United States. The seasonal dependence of this relationship is also reproduced by the model.

1. Introduction

The dominant pattern of observed sea surface temperature (SST) variability in the North Pacific is referred to as the "Pacific Decadal Oscillation" (PDO) (Mantua et al. 1997). The PDO has substantial decadal-scale variability, with characteristic time scales in the observed record of 15-25 years and 50-70 years (Minobe et al. 1997). The PDO spatial pattern associated is characterized by a "horseshoe" shape, with SST anomalies of one sign in the central and western North Pacific, and SST anomalies of the opposite sign in the east extending northwestward to the North American coast and southwestward to the central tropical Pacific (Figs. 1a, b) (Mantua et al. 1997). This decadal SST variability is associated with fluctuations of the Aleutian low and mid-latitude westerly winds (Figs. 1a, b) (e.g., Nakamura et al. 1997). The PDO variations over the last century can be clearly seen from the PDO index time series, shown in Fig. 1c. A significant climate shift appears in 1976/1977, with a shift from negative to positive SST anomalies in the tropical eastern Pacific and eastern North Pacific (Fig. 1). This apparent "regime shift" was associated with a large-scale change in the physical climate system and in marine ecosystems, as well as with climatic variations over North America, including air temperature, precipitation, streamflow and vegetation (Cayan et al. 2001; Deser et al. 2004). There would be enormous societal benefits if such PDO swings could be accurately predicted.

Several hypotheses have been proposed for the origin of the PDO, including North Pacific coupled ocean-atmosphere interactions (e.g., Latif and Barnett 1994, 1996; Wu et al. 2003; Zhong et al. 2008, 2009), an integrating effect of the ocean on

high-frequency atmospheric variability (e.g., Jin 1997; Pierce et al. 2001; Newman et al. 2003) and teleconnections between the tropics and extratropics (e.g., Gu and Philander 1997; Schneider et al. 1999). However, model results sometimes are inconsistent with observational evidence.

Observational analyses show that the PDO has largest SST anomalies in the central North Pacific, with a weaker secondary maximum of SST variability located along the Kuroshio-Oyashio Extension (KOE) (Figs. 1a, b). Both observational analyses and the results from ocean modeling studies have suggested that different physical processes determine the decadal-scale evolution of SST in these two regions (e.g., Deser et al. 1996; Xie et al. 2000). In the central North Pacific the SST anomalies are primarily determined through the strength of the westerly wind and associated changes in the Ekman transport. SST anomalies in the KOE region appear to be more strongly influenced by a meridional displacement of the boundary between the subpolar and subtropical gyres.

Observational and ocean-only modeling studies, however, are not able to provide much insight into the role of ocean to atmosphere feedback for PDO variability. In this regard, coupled ocean-atmosphere models are very powerful tools. In a pioneering early work, Latif and Barnett (1994) suggested that the PDO can be attributed to ocean-atmosphere interactions involving the subtropical ocean gyre circulation and the Aleutian low pressure system. However, some aspects of their proposed mechanism do not appear to be completely consistent with observations and ocean model results. For example, Schneider et al. (2002) found that the SST

variability in the KOE region lagged wind variability in the central Pacific by about 5 years and the delayed time scale is mainly due to the first baroclinic Rossby wave. In Latif and Barnett (1994), the central Pacific SST anomaly followed that of KOE region, with the central Pacific ocean responding passively to overlying atmosphere shift that are affected by KOE conditions. This inconsistency primarily arises from what the origin of atmosphere circulation shift is and/or how the atmosphere responds to local and remote SST anomalies in observation and models. Seager et al. (2001) and Qiu et al. (2014) suggested that a meridional shift, rather than strength change of the subtropical gyre circulation is responsible for the SST anomalies in the KOE region. Moreover, in both observations and ocean models, the heat flux tends to damp the SST anomalies over the North Pacific Ocean (Deser et al. 1996; Seager et al. 2001; Kelly and Dong 2004), which is contrary to the results of Latif and Barnett (1994). It is expected that the ECHO model used in Latif and Barnett paper underestimates the SST feedback on the heat flux and thus generates a positive correlation between the SST and heat flux on decadal time scales as proposed by Zhong and Liu (2009). Kwon and Deser (2007) suggested a more realistic mechanism for the PDO using CCSM2. They suggested that decadal SST variability in the KOE region is mainly forced by convergence/divergence of horizontal heat transport associated with the geostrophic flow. Local surface heat fluxes tend to damp the SST, while the Ekman heat flux divergence acts as a positive feedback. Nevertheless, the positive contribution of Ekman heat flux divergence to the central Pacific SST anomaly in their study mainly arises from the meridional temperature gradient

anomaly, rather than the anomalous Ekman current, in sharp contrast to observational analyses (Seager et al. 2001). d'Orgeville and Peltier (2009) further confirmed that the PDO cycle is accompanied by a meridional shift of the Aleutian low and KOE axis based on the coupled model CCSM3. In their analyses they suggest that the phase reversal of the PDO is strongly linked with feedbacks from sea ice changes in the northernmost parts of the basin. The potential importance of the subpolar gyre in the PDO was also proposed in Zhong and Liu (2009) using the same coupled model, although the latter focused on the PDO multidecadal peak (50-70 year), while the former (d'Orgeville and Peltier 2009) focused on the PDO decadal peak (15-25 year).

Generally speaking, the physical mechanisms of the PDO are still under debate. In the current paper, we examine the PDO in long preindustrial control simulations using several different models developed at the Geophysical Fluid Dynamics Laboratory (GFDL). The models differ in physics and resolution. The purpose of this study is to take advantage of these long integrations and the suite of GFDL models, including high resolution models, to investigate unresolved issues regarding the PDO, including the positive and negative feedbacks of the PDO, the processes that determine the decadal time scale of the PDO, the role of air-sea coupling in the tropics and the role of stochastic forcing. The paper is arranged as follows: section 2 describes the models, observational datasets and sensitivity experiments. Section 3 presents the PDO characteristics in all GFDL models. The role of atmosphere stochastic forcing and tropical air-sea coupling is examined in section 4. In section 5, we examine the physical mechanisms of the PDO. The impact of PDO on North

American precipitation is investigated in section 6. We conclude in section 7 with a discussion and summary.

2. Models and observational datasets

Several versions of GFDL coupled ocean-atmosphere climate models are used in this study, including CM2.1, CM2.5_FLOR, CM2.5_FLOR_FA, CM2.5, CM2.6 and CM3. Some of the defining characteristics of the models are summarized in Table 1. The use of such a wide variety of models allows some assessment of the robustness of the PDO characteristics. All of the models have 50 levels in the ocean. We make use of multi-century control simulations available with each of the models (200-yr for CM2.6 and 800-yr for the rest models), using constant atmospheric composition and radiative forcing in 1860. These long control simulations are used to estimate the inherent internal variability of the models. We note that the CM2.5_FLOR_FA model (Vecchi et al. 2014) uses flux adjustments. This technique is used to explore the model sensitivity to artificially reducing model bias at least in the ocean surface. Further details on the models are available in the references for each model.

To assess whether atmospheric stochastic noise forcing is sufficient to generate the PDO, or whether active two-way ocean-atmosphere coupling is essential, we perform a sensitivity experiment using CM2.5_FLOR in which air-sea coupling is altered over the entire Pacific Ocean (30^{o}S-80^{o}N, 100^{o}E-80^{o}W). We choose this model because it has relatively high resolution in the atmosphere, and yet is computationally efficient so that multiple sensitivity simulations can be conducted. In this experiment, called “stochastic run”, the model atmosphere over the Pacific “sees”

only a repeating seasonal cycle of SSTs rather than the SSTs calculated by the ocean component of the coupled model. Therefore, fluxes from the ocean to the atmosphere over this region contain no information on any ocean variability beyond a repeating seasonal cycle, and there is no direct coupled feedback possible. In turn, the fluxes from the atmosphere to the ocean are coming from an atmosphere that has no "knowledge" of the variability occurring in the model Pacific Ocean, apart from the seasonal cycle. The technique used here is the same as Wu et al. (2003) and Zhong and Liu (2008).

To investigate the possibility that the Tropics are responsible for driving the PDO, we conduct an additional sensitivity experiment using CM2.5_FLOR which is called "TPAC_RESTORE". This experiment is identical to the fully coupled control simulation, except that SSTs in the tropical Pacific (equatorward of 20^o) are restored to their climatological seasonal cycle with a restoring time scale of 5 days. The impact of tropical Pacific variability generated through air-sea interaction, such as ENSO, is therefore effectively removed. In the extratropics poleward of 20^o, full ocean-atmosphere coupling remains active as in the control run. Both of the "stochastic" and "TPAC_RESTORE" runs are integrated for 300 years.

Several observational and reanalysis datasets are used to evaluate the model results. We use an extended reconstructed SST (ERSST) data set on a $2^o \times 2^o$ grid from 1854 to 2013 (Smith and Reynolds 2004). We use the atmospheric reanalysis product for the 20th century, designated as 20CRv2. The reanalysis output extends from 1871 to 2010, with output available at 2° spatial resolution (Compo et al. 2011). We also

use the Met Office Hadley Center's sea level pressure HadSLP2, available on a $5^o \times 5^o$ grid from 1850 to 2004 (Allan and Ansell 2006). Finally, we use high resolution ($0.5^o \times 0.5^o$) precipitation time-series dataset spanning the period 1901-2012, available from the Climatic Research Unit of the University of East Anglia.

3. The PDO characteristics in all versions of GFDL model

The PDO spatial patterns in different GFDL model versions are shown in Fig. 2 as the regressions of SST and surface wind stress on the PDO index. Here the PDO index is defined as the normalized principal component of the leading EOF of annual mean SST over the North Pacific Ocean (20^oN-60^oN, west coast to east coast). In general, the PDO spatial pattern shares great similarities among the different GFDL models, albeit with some differences in amplitude. The SST anomaly associated with the PDO is characterized by a horseshoe-like pattern over the North Pacific, with SST anomalies of one sign in the western and central North Pacific, surrounded by anomalies of the opposite sign along the west coast of North America. This PDO horseshoe-like pattern is broadly similar to that seen in observational analyses, although the observed pattern has its primary maximum in the central North Pacific along with a weaker secondary maximum along the KOE region (e.g. Deser and Blackmon 1995). All models tend to have their maximum amplitude over the KOE region (Fig. 2 versus Fig. 1a). The CM2.5_FLOR model also has a secondary maximum over the central North Pacific (Fig. 2b). The positive (negative) SST anomalies extend from the eastern North Pacific to the central equator Pacific during

the PDO warm (cold) phase. The anomalies are weaker in all the models than those shown in observational analyses (Fig. 1a versus Fig. 2).

In the PDO warm (cold) phase, the Aleutian Low is strengthened (weakened) and shifts southward (northward) (Fig. 2), which strongly resembles the observations (Fig. 1a). The PDO spatial pattern also shows significant amplitude in the tropics, although the magnitude is smaller than in the North Pacific (Fig. 2). During the PDO warm (cold) phase, the tropical Pacific is characterized by an El Niño-like (a La Niña-like) warming (cooling) and dominated by a westerly (easterly) wind anomaly. A close examination finds that the maximum SST response over the tropics extends too far west in all the models as compared to observations (Fig. 1a versus Fig. 2). Moreover, the tropical Pacific response in CM2.5_FLOR is much stronger than that in observations (Fig. 1a versus Fig. 2b). Both biases are commonly seen in El Niño Southern Oscillation (ENSO) simulations by coupled models (Delworth et al. 2012). The PDO-related SST anomalies in the tropical Pacific suggest that ENSO variability may play a role in the PDO dynamics.

We show a power spectrum analysis of the annually PDO index in Fig. 3 (we obtain similar results when we use the annual SST time series averaged over the KOE region (KOEI; 35^{o}-45^{o}N, 140^{o}-200^{o}E)). This shows that the PDO has an approximately 20-year period in all the models. This approximate 20-yr time scale can be also found in observations and paleoclimate records (e.g., Minobe et al. 1997; Biondi et al. 2001; Gedalof et al. 2002), indicating that the GFDL models reproduce a realistic time scale for the PDO. It is worth noting that a second time-scale for the

observed PDO, at around 50-70 years, is not captured by the GFDL models. In the following sections, we will focus on the PDO's quasi-20-yr peak. Given that all the models have similar behaviors for the PDO, we show analyses using the CM2.5_FLOR model.

4. The role of atmosphere stochastic noise and tropical air-sea coupling in PDO using CM2.5_FLOR

We now assess whether atmospheric stochastic noise forcing is sufficient to generate the PDO, or whether active two-way ocean-atmosphere coupling is essential. In this stochastic run, variability in the atmosphere over the Pacific is generated predominantly by internal atmospheric processes, rather than as a response to local oceanic variations. Without air-sea coupling in the entire Pacific Ocean, SST variability in the tropical Pacific is reduced by about 90% as compared to the fully coupled control simulation, while it is only reduced by 20% in the extratropics (Fig. 4c). This is not surprising, since tropical SST variability is mainly due to strong air-sea feedbacks, whereas extratropical SST variability is largely dominated by stochastic noise forcing (Liu 2012). The dominant pattern of SST variability in the North Pacific Ocean is a PDO-like mode which also appears in the control simulation (Fig. 4a). The dominant atmospheric variability mode over the North Pacific is also similar to that in the control run (Fig. 5a versus Fig. 5c). However, the temporal behavior of the PDO is significantly different in these experiments. In the absence of local ocean-atmosphere coupling in the stochastic run, SST and SLP variations over the North Pacific Ocean have no preferred bidecadal time scale, as shown in Fig. 4b

and Fig. 5d. This can be compared to the PDO characteristics in control run which has a pronounced decadal peak of 20-yr (Fig. 3b and Fig. 5b). Thus, atmospheric stochastic forcing can generate a PDO-like spatial mode, but without significant bidecadal variability. In other words, ocean-atmosphere coupling is critical to establishing the decadal-time scale of the basin-scale PDO.

To investigate the possibility that the tropical air sea coupling is responsible for driving the PDO, we conduct an additional experiment called "TPAC_RESTORE". Fig. 4f shows zonal means of the Pacific annual mean SST standard deviation (std) in both the control and TPAC_RESTORE simulations. As expected, SST variability is drastically reduced in the tropical Pacific with the strong SST restoring. SST variability in the North Pacific is slightly weaker than in the control simulation, but the difference is not significantly different. In TPAC_RESTORE, the dominant mode of extratropical SST variability is still characterized by the PDO-like structure (Fig. 4d). However, the TPAC_RESTORE mode is more zonally-oriented and only has one center compared to the two centers in control run (Fig. 2b), with intensified variability toward the western coast along 40^{o}N. This difference in the pattern of variability is apparently related to the absence of tropical-extratropical positive feedback (e.g., Deser and Blackmon 1995; Zhong and Liu 2008). The spectrum of the KOE SST time series is shown in Fig. 4e, and is characterized by a quasi-20-yr peak (above 95% confidence level). In the extratropical atmosphere, the PDO mode corresponds to a PNA-like SLP pattern which is also represented by a quasi-20-yr peak in the control run (Figs. 5a, b). This phenomenon is still retained in TPAC_RESTORE (Figs. 5e, f).

The comparison between the PDO mode in the control simulation and TPAC_RESTORE demonstrates that the model PDO originates primarily from processes in the extratropical coupled air-sea system, rather than as a remote response from the tropics. Tropical air-sea coupling slightly increases the PDO amplitude and plays a significant role in the central North Pacific SST variability.

5. PDO mechanisms in CM2.5_FLOR

The sensitivity experiments above indicate that the PDO in GFDL model is primarily attributed to the coupled air-sea interaction in the Pacific extratropics. Then, the question is how is the extratropical ocean and atmosphere coupled? To better answer this question, we examine the life cycle of PDO in CM2.5_FLOR, including the subsurface processes and heat budgets in key regions. We also pay special attention to potential positive and negative feedbacks that are important for establishing the quasi-oscillatory behavior of the PDO seen in the models.

a. Life cycle of the PDO

The evolution of temperature anomalies associated with the PDO is shown as the lagged regression map of SST upon the PDO index (Figs. 6a-g). To focus on decadal variability (20-yr peak), all data are first 10-30-yr band-pass filtered prior to regression. At a lag of 0yr, the PDO is in its mature warm phase, with negative SST anomalies in the western and central North Pacific, and positive SST anomalies in most of the rest of the North Pacific (Fig. 6a).

We characterize the evolution of the PDO by the regression coefficients at various lags. As we move forward from lag 0, the positive SST anomaly in the

western subpolar gyre grows and gradually extends southward into the mid-latitude KOE region, while the negative SST in the KOE region gradually decays (Figs. 6a-e). A positive SST anomaly emerges in the western subtropics at a lag of 2yr (Fig. 6c). This western subtropical warming then intensifies and spreads northward into the mid-latitudes (Figs. 6c-e). At a lag of 4yr, a positive SST anomaly appears in the central North Pacific, and then grows and spreads westward to the KOE region (Figs. 6d-e). At a lag of 8yr, the phase of the PDO is completely flipped (Fig. 6f). The positive SST anomaly over the KOE region then amplifies, leading to a mature cold phase of the PDO at a lag of 10yr (Fig. 6g).

Negative SST anomalies, that had emerged in the northeastern Pacific Ocean around a lag of 4yr (Fig. 6d), subsequently grow, expand northwestward along the North American coast (Figs. 6d-f), and eventually form the large-scale pattern of negative SST anomalies that surround the positive SST anomalies in the central and western North Pacific (Fig. 6g). The surface heat flux tends to damp the SST anomaly (Figs. 6a-g, shown by contours), implying a dominant role of ocean dynamics in the PDO evolution on decadal timescales.

During the PDO cycle, the atmosphere circulation undergoes significant changes as shown in Figs. 6h-n. The mature warm phase of the PDO at a lag of 0yr corresponds to a strengthening and southward shift of the Aleutian low (Fig. 6h). The subtropical high also shows a slight strengthening and southward shift. Due to these changes the wind stress curl anomaly is characterized by a dipole structure, with a positive anomaly over the subpolar and mid-latitudes and a negative anomaly over the

subtropics. This wind stress curl pattern associated with the PDO is consistent with that seen in observations (See Fig. 5 in Wu et al. 2005). Note that the positive wind stress curl anomaly crosses the long term mean zero wind stress curl line, which can induce a southward movement of the subtropical and subpolar gyre boundary (Fig. 7). As the negative SST anomaly weakens over the KOE region (at lag 1yr), the positive wind stress curl anomaly also weakens and gradually retreats northward (Fig. 6i). At the same time, an anomalous anticyclonic wind/negative wind stress curl anomaly emerges in mid-latitudes (Figs. 6i, j), which tends to expand and amplify, eventually occupying the entire mid-latitude and subpolar region (Figs. 6i-n). Moreover, a positive wind stress curl gradually forms in the subtropics (Figs. 6k-n). At lags of 4-10yr, the wind stress anomaly pattern is completely reversed, as characterized by a weakening and northward shift of the Aleutian low, corresponding to a cold phase of the PDO (Figs. 6k-n). Due to the northward shift of the Aleutian low, the subtropical and subpolar gyre boundary moves northward (Figs. 7o-u).

The relative phasing of SST anomalies in the western subpolar, subtropic and KOE region can be seen more clearly from the subsurface profile (Fig. 7). We show in Fig. 7 lagged relationships of temperature, salinity, and zonal velocity versus the PDO index, plotted as a function of depth (Figs. 7a-n). A positive temperature anomaly appears in the subsurface subpolar region at a lag of 0yr (Fig. 7a), which then expands to the surface (Fig. 7b, c) by the mean upwelling forced by the wind, amplifies (Fig. 7d, e) and propagates southward along the Oyashio in the top 100m (Figs. 7b-e), eventually leading to a positive SST anomaly in the KOE region (Fig.

7e). At a lag of 10yr, a cooling anomaly appears in the subpolar subsurface (Fig. 7f, g); this negative temperature anomaly will play a role in an eventual switch of the KOE SST back to colder than normal conditions. The salinity evolution in the mid-latitudes and subpolar region is almost in phase with the temperature evolution, particularly in the subsurface (Figs. 7a-g versus Figs. 7h-n). This suggests a potentially significant role for convective instability (Zhong and Liu 2009).

We use lagged regressions (Figs. 8a, b) to show that the subsurface subpolar anomaly leads the surface subpolar anomaly by about 5years, and the surface subpolar anomaly leads the KOE anomaly by another 5years. The sum of these two leads accounts for a half cycle of the PDO (~ 10yr). The subpolar evolution here is very similar to that found in the CCSM3 model (Zhong and Liu 2009), although in their study they focus on the PDO multidecadal variability.

In the subtropics, we show (Figs. 7a-e) that a positive temperature anomaly first appears in the subsurface subtropical region, gradually intensifies and finally peaks at a lag of 6yr. The subsurface warming anomaly is then entrained to the surface and advected northward by the Kuroshio, leading to a phase reversal of the SST anomaly over the KOE region (Figs. 7d-g). Fig. 8c further confirms that the subsurface subtropical temperature leads the surface subtropical SST anomaly by about 2 years, and the latter leads the KOE SST anomaly by another 3 years. In contrast to the subpolar region, the sum of these two leads equals 5 years, and that accounts for a quarter of PDO cycle.

After positive SST anomalies spread from the western subtropical and subpolar regions to the KOE, the KOE negative SST anomaly gradually decays (Figs. 6c, d). This corresponds to an anomalous anticyclonic wind/negative wind stress curl over the North Pacific. This surface wind shift coincides with a central North Pacific warming and then a KOE warming after a 3-5year delay (mid-latitude pathway). To understand the processes responsible for driving decadal SST variability over these two regions (marked by rectangles in Fig. 6a), we examine the local heat budget over the upper 100m, calculated as follows:

$$\frac{\partial \mathrm{T}}{\partial \mathrm{t}} = \frac{Q_{net}}{\rho_o c_p H} - u\frac{\partial \mathrm{T}}{\partial \mathrm{x}} - v\frac{\partial \mathrm{T}}{\partial \mathrm{y}} - w\frac{\partial \mathrm{T}}{\partial \mathrm{z}} + Residual \quad (1)$$

where T is the ocean temperature, Q_{net} is the net air-sea surface heat flux (positive downward), H is mixed layer depth assumed to be 100 m constant, ρ_o is seawater density, C_p is the specific heat of seawater, u is the zonal velocity, v is the meridional velocity and w is the vertical velocity. All the terms not explicitly listed, including horizontal and vertical diffusion, and convection, are included in a Residual term. Over the KOE region, the decadal SST anomaly is primarily associated with meridional temperature advection, whereas heat flux and zonal and vertical temperature advection act as damping terms (Fig. 9a). A decomposition of the meridional advection term finds that temperature advection by the anomalous meridional current is dominant. We further decompose temperature advection by the anomalous meridional current into the contributions from anomalous meridional geostrophic current and from the anomalous Ekman current. Here, the Ekman meridional temperature advection integrated in the Ekman layer is estimated by

$C_p \frac{\tau_x}{f} \frac{\partial T_{EK}}{\partial y}$, where C_p is specific heat for water, τ_x is zonal wind stress, f is Coriolis force and T_{EK} is the vertically averaged ocean temperature within the Ekman layer (can be estimated by the mixed layer suggested by Wijffels et al. 1994). This shows that temperature advection in the KOE region is dominated by the anomalous meridional geostrophic current, which is attributed to the meridional shift of the confluence of the subtropical and subpolar gyres (Fig. 7o-u) due to the wind stress curl anomaly several years prior (Fig. 6h-n). Similarly, decadal SST fluctuations over the central Pacific Ocean are largely generated by temperature advection by the anomalous meridional current and strongly damped by the heat flux (Fig. 9b). However, this anomalous meridional current is dominated by the Ekman component, in sharp contrast to the KOE region (Fig. 9a versus Fig. 9b). The central North Pacific SST anomaly leads that in the KOE regions by about 3-5 years (Figs. 9a, b), which is consistent with the PDO SST cycle (Figs. 6a-g).

In contrast to the KOE region and central North Pacific Ocean, the contributions from anomalous meridional geostrophic and Ekman currents to the northeastern Pacific SST anomalies are comparable in magnitude (Fig. 9c). The anomalous cyclonic (anticyclonic) wind drives an anomalous northwestward (southeastward) current along the North American coast, which creates positive (negative) temperature advection from the relatively low (high) latitudes to high (low) latitudes and in turn generates a warm (cold) anomaly there.

The above heat budget analysis points out that the heat flux mainly damps SST anomalies over the North Pacific during the PDO cycle. This conclusion cannot be

totally held if we use the unfiltered data. We found that the heat flux favors the SST phase transition over the central North Pacific and Northeastern Pacific Oceans on rapid time scales. The phase reversals in these two regions are favored by the sustained heat flux anomalies during a short period preceding the shift (not shown). This is consistent with the argument proposed by Miller et al. (1994). Over the KOE region, the surface net heat flux damps the SST anomaly even in the unfiltered data, indicating a dominant role of ocean dynamics.

The time evolution of temperature, salinity, and surface wind suggests three key pathways for the PDO cycle: the subpolar pathway, the subtropical pathway and the mid-latitudes pathway (central North Pacific to KOE region). In the next section, we will examine the overarching physical mechanism.

b. Physical mechanisms controlling the life cycle of PDO

i. Overview of the PDO mechanism

The physical processes involved in a life cycle of the PDO are illustrated with a schematic diagram shown in Fig. 10 (based on Zhong and Liu, 2009, and modified to show the mechanisms operating in the GFDL models). We start with the PDO in its' mature warm phase (Fig. 10a). The mid-latitude and western subtropics exhibit maximum negative temperature anomalies, whereas the subsurface western subpolar ocean shows significant positive temperature anomalies. The atmosphere is characterized by a strengthened and southward shifted Aleutian low and subtropical high.

Then the system begins the transition to the opposite (cold) phase of the PDO. The subsurface subpolar positive temperature anomalies gradually upwell to the surface, grow and then propagate southward with the Oyashio (Fig. 10b). In addition, at a lag of ~5yr the subsurface western subtropical ocean displays a significant warming. This occurs in response to anticyclonic wind anomalies over the preceding several years, as shown in Fig. 10a. This subsurface subtropical warming is then entrained into the surface and advected northward to the KOE region (Fig. 10b). The warm SST anomalies advected from the western subpolar and subtropical regions contribute to a decay of the original KOE negative SST anomaly and the formation of a tripole SST structure (Fig. 6d). This in turn induces an anomalous anticyclonic wind anomaly in the mid-latitudes. This anticyclonic wind anomaly warms the central Pacific first through anomalous northward Ekman transport, and then through an anomalous wind stress curl pattern that leads to a northward shift of the subtropical and subpolar gyre boundary through the adjustment to wind stress induced Rossby wave forcing (Fig. 10b). After the subpolar, subtropical and central Pacific positive temperature anomalies spread to the KOE region, the positive SST anomaly over the KOE is amplified through convective feedback (Zhong and Liu 2009) and can be advected to the central Pacific region (Fig. 10c). The large area of positive SST anomalies over the KOE and central North Pacific regions can further feedback to the atmosphere, inducing a positive air-sea feedback to amplify the initial warming there (as will be shown later). At a lag of 10 year, a mature cold phase of the PDO is fully established (Fig. 10c).

Two processes are important in the transition back to the warm phase of the PDO (Fig. 10c). We note that in the previous warm phase of the PDO negative SST anomalies in the KOE region induced anomalous cyclonic winds and upwelling over the subpolar region (Fig. 10a). This anomalous wind forcing created a westward propagating internal wave, with a very slow phase speed (decades to cross the basin) related to the weak stratification and high latitude. This upwelling wave induces a cold fresh anomaly in the subsurface subpolar region approximately a decade after the wind stress forcing (Fig. 10c). This subsurface cold anomaly in the subpolar gyre is present in the cold phase of the PDO but was generated by wind stress anomalies in the previous warm phase of the PDO. This subsurface cold anomaly is one of the precursor conditions that help to flip the PDO back to the warm phase by upwelling to the surface and subsequent southward propagation to the KOE region. The other process important for flipping the PDO phase comes from the subtropical region, where positive wind stress curl anomalies are present in the cold phase of the PDO (see Fig. 6n). This stress induces Rossby waves that lead to cooling of the western subtropical gyre. Both factors (in the subpolar and subtropical gyres) favor the entire system going into the other half of the cycle (Figs. 10c, d). Thereby, a closed loop of the PDO is established in the form of a coupled air-sea interaction in the extratropics. In the following section we will explain each process described above in detail.

The above PDO mechanism in GFDL model shares some similarities with the NCAR CCSM2 model (Kwon and Deser 2007), both of which arise from North Pacific air-sea interaction. However, the time scale of the PDO in GFDL models is a

little longer than in the NCAR model, with the former of 20-yr and the latter of 15-yr. The subtropical and subpolar pathways in the GFDL model that contribute delayed negative feedbacks during the PDO cycle are absent in the NCAR model. In the GFDL model, the western subtropical and subpolar SST anomalies generated by the subtropical/subpolar pathways are advected to the mid-latitude region, leading to a tripole SST formation that subsequently feedbacks to the atmosphere and further triggers the mid-latitude pathway. Therefore, the subtropical/subpolar and mid-latitude pathways in the GFDL model are both important during the PDO cycle. In NCAR model, we only see the mid-latitude pathway, in which the large area SST warming in the KOE and central North Pacific (mature cold phase of PDO) induces a low pressure response in the North Pacific that can create a westward upwelling Rossby wave along 40^{o}N to flip the PDO phase.

ii. Further examination of important process in each phase

We first examine the subpolar pathway. The physics behind this pathway are similar to Zhong and Liu (2009), except that the wave propagation time scale in the GFDL model is much shorter than in CCSM3. As suggested by Zhong and Liu (2009), the strong relationship between the KOE region and the subsurface subpolar ocean is through the atmosphere bridge. Fig. 11 shows analyses regarding the characteristics of North Pacific air-sea coupling. The result shows a strong relationship when geopotential height anomalies (GHT) lead SST, but a much weaker relationship when SST leads (Fig. 11a, b). For example, positive GHT anomalies in the subpolar gyre tend to weaken the westerly winds, and thus induce a warming

anomaly over the KOE through reduced latent heat flux and anomalous northward Ekman transport. The positive SST anomalies can impact the atmosphere to some degree, inducing an equivalent barotropic ridge that will amplify the initial warm anomaly. This suggests that the North Pacific Ocean is dominated by a weak positive air-sea feedback, consistent with observations (Frankignoul and Sennéchael 2007).

The mid-latitude SST feedback to the atmosphere can be seen from simulations in which we impose SST anomalies corresponding to the mature cold phase of the PDO (north of 20^{o}N) (Fig. 6g) in the coupled model. We performed two sensitivity experiments. The first run is control restoring experiment in which we restore the model output SST at every step to the climatological SST seasonal cycle in control simulation over the entire Pacific Ocean (30^{o}-80^{o}N, 120^{o}-280^{o}E), while the ocean and atmosphere are fully active elsewhere. The other experiment is the same as the first run, but with the SST in the Pacific Ocean restoring to an SST field that is the sum of the seasonal cycle from the control simulation plus the SST anomaly north of 20^{o}N derived from the mature cold phase of PDO (Fig. 6g). Both runs are integrated for 20 years and the last 10 years differences are taken as the response. A 100-member ensemble run is performed with each experiment starting from an equilibrium state of a long fully coupled control simulation, and the ensemble-mean response is shown. In response to a warm SST anomaly in the North Pacific, SLP/surface wind stress shows a high/anticyclonic anomaly in the subpolar and mid-latitude (Fig. 12a, b), representing a weakening and northward shift of the Aleutian low. The subtropical high also shows a slight weakening. Accordingly, the wind stress curl anomaly has a

dipole structure, with a strong negative curl in the north and a weak positive curl in the south. This atmosphere response is consistent with the regression analysis (Fig. 11). We also found the magnitude of ocean feedback to the atmosphere (short time scale (within 1 year), Fig. 11d) is comparable to the atmosphere forcing of ocean on decadal time scales (Fig. 11c).

The persistent negative wind stress curl due to warm KOE SST feedback over the subpolar ocean (Fig. 11d) induces a downward Ekman pumping and depresses the thermocline or halocline, as suggested by Schneider et al. (2002). The anomaly then propagates westward across the basin via Rossby waves, leading to a warm anomaly in the subsurface western subpolar region. This wind-forced westward response can be clearly seen in the heat content propagation in the upper 400m at 50^{o}N, but mainly confined west of 160^{o}W (not shown) where the maximum wind stress curl anomaly occurs (Fig. 6h and Figs. 11c, d). Fig. 13a exhibits a lead-lag correlation between the PDO index and the subsurface western subpolar temperature anomaly, which shows a negative correlation as low as -0.45 when the PDO leads subsurface subpolar temperature anomaly by 8-10 years and a positive correlation (0.43) at zero lag. The simultaneous positive correlation is clearly seen from Figs. 7a. The negative correlation implies that a positive wind stress curl anomaly over the subpolar region associated with the positive PDO index can lead to a cold subsurface western subpolar Pacific after 10 years, and vice versa. To further confirm this delay time scale we performed a sensitivity experiment. This is similar to the control simulation except that, at each time step, the ocean component of the model feels an additional wind

stress anomaly that corresponds to the PDO warm phase (Fig. 6h). Note that the additional wind stress anomaly only affects the momentum flux, not the latent and sensible heat fluxes. This anomaly is intended to isolate the model's response to the PDO stress pattern, and is only applied over the North Pacific (20^{o}-65^{o}N, west coast to east coast). A 10-member ensemble experiment is performed. To increase the signal-to-noise ratio, the wind stress anomaly is amplified by a factor of three.

Fig. 14 shows the ensemble mean response for 1-10yr adjustment of SST (left panel) and zonal mean temperature (right panel) to the anomalous wind stress. Forced by the anomalous cyclonic wind, the central Pacific SST cools first at year 1 (Fig. 14a), and then the KOE regions cools (Fig. 14b). The former response is due to the anomalous southward Ekman transport, which is local and fast, while the latter is associated with the delayed baroclinic Rossby wave adjustment. This mid-latitude ocean response is consistent with the heat budget analysis (Figs. 9a, b). In the subpolar region, significant subsurface cooling appears by the tenth year (Fig. 14f), which is in agreement with the lead-lag correlation (Fig. 13a). This subsurface western subpolar Pacific delayed response to the wind is attributed to the subpolar ocean baroclinic adjustment. We calculate the first baroclinic Rossby wave speed in the North Pacific according to the approach of Chelton et al. (1998), shown in Fig. 15. At 50^{o}N, the estimated speed is 0.90 cm/s, equivalent to a cross-basin time scale of ~26 yr. In the GFDL model, the maximum wind stress curl anomaly in the subpolar region is located around 160^{o}W. Therefore, Rossby wave propagation takes about half of the cross-basin time (~10 years).

Similar to the subpolar pathway, the connection from the KOE to the subsurface western subtropical ocean is primarily through the atmospheric bridge. As shown in Fig. 6h and Fig. 12a, a warm phase of the PDO is accompanied by a modest strengthening and southward retreat of the subtropical high. This generates a negative wind stress curl anomaly in the 20^{o}N-30^{o}N band of the subtropical region, which can induce warming in the subsurface western subtropical Pacific via Rossby wave propagation. The lead-lag correlation between the PDO index and the subsurface western subtropical temperature (Fig. 13b) shows a positive correlation (0.45) when the PDO index leads the subsurface temperature by about 5 years. This delayed subtropical gyre adjustment is further verified by the sensitivity experiment previously discussed (Fig. 14). Forced by a wind stress anomaly during the PDO warm phase, a significant warming emerges in the subtropical subsurface after about 5 years (Fig. 14e). Around 25^{o}N, the estimated Rossby wave speed is 3 cm/s, equivalent to a cross-basin time scale of ~8 yr (Fig. 15). Note that the maximum wind stress curl anomaly in the subtropical region associated with the PDO mature phase is mainly located west of 140^{o}W (Fig. 6h). Therefore, the Rossby wave propagation takes about two thirds of the cross-basin time (about ~5 years).

The tripole SST structure in the mid-latitudes with a narrow cooling in the KOE region surrounded by warming anomalies to the north and south favors a trapped surface high pressure over the KOE region (Fig. 6j). This local atmospheric response is further confirmed by the sensitivity experiment when we prescribe the tripole SST (Fig. 5d) over the North Pacific Ocean (Fig. 12c, d). This wind anomaly first causes a

central Pacific warming as a result of anomalously strong Ekman northward transport. The negative wind stress curl anomaly over the mid-latitudes subsequently drives a poleward shift of the subtropical-subpolar gyre boundary after Rossby wave adjustment, and finally generates a warming in the Kuroshio off Japan. To further confirm the ocean delayed response to this wind anomaly, we calculate the regression of surface wind stress and wind stress curl upon the KOE SST index with the wind leading 1-10 years. The lag regressions demonstrate that significant basin-scale wind stress curl anomalies precede the KOE positive SST anomaly with maximum when the wind stress curl leads by 5yr (Fig.11c). This delay time is consistent with that in Seager et al. (2001). The increasing positive SST anomalies over the KOE region can spread further over the North Pacific by the mean zonal current, which tends to amplify the initial central Pacific warming.

6. Impact of the PDO on North American hydroclimate

We show precipitation anomalies associated with the PDO in Northern Hemisphere warm (April-September) (Fig. 16) and cold (October-March) (Fig. 17) seasons in both the model and observations. The model results are broadly in agreement with the observations, with wet (dry) conditions in the southwestern U.S. and northern Mexico during the PDO warm (cold) phase in both seasons. Further examination finds that the dominant precipitation anomaly is more trapped over the central (southwestern) U.S. in the warm (cold) season in both model and observation. During the PDO warm (cold) phase, the atmospheric response shows a classic positive (negative) phase of the Pacific North Atlantic (PNA) teleconnection (Horel

and Wallace 1981), with a low (high) pressure in the North Pacific, a high (low) pressure over the North America and a low (high) pressure over the southern U.S. The anomalous southerly (northerly) wind over the southwestern U.S. enhances (decreases) moisture transport from south to north and therefore leads to enhanced (reduced) precipitation. Over the southern U.S., anomalous cyclonic (anticyclonic) wind acts to increase (decrease) moisture convergence and thus produces an increase of precipitation there.

7. Discussion and summary

North Pacific decadal variability is studied in a suite of GFDL climate models of varying resolution, including a version with an eddy resolving ocean (0.1^{o} ocean grid spacing) and multiple versions with 50-km atmospheric grid spacing. A PDO-like pattern, with a characteristic 20-year timescale, is the dominant mode of extratropical North Pacific SST variability in all the models.

We conclude from sensitivity experiments that while the amplitude and some details of the structure of the PDO are influenced from the Tropics, the PDO in our models is primarily generated by processes local to the North Pacific. Further, we find that coupled air-sea interactions, in which the atmosphere responds to the state of the ocean in the North Pacific, are essential for setting the decadal timescale of the PDO. The spatial structure of the PDO, at least in terms of SST, can be generated from atmospheric internal variability alone, but ocean-to-atmospheric feedback in the extratropics appears to be necessary to generate the 20-year timescale.

We examine one model in detail to evaluate the mechanism of the simulated PDO (section 4). We find that a number of factors contribute, including: extratropical air-sea interaction, propagation of internal oceanic Rossby waves, ocean convective feedback, and shifts in the boundaries of the subtropical and subpolar gyres in response to wind stress changes. Of particular importance in setting the approximately 20 year time scale are the 5-10 years that Rossby waves take to propagate westward at various latitudes over subsections of the western North Pacific. We find that three pathways are particularly important, involving both the subtropical and subpolar gyres, as well as propagation at mid-latitudes.

The proposed subpolar and subtropical pathways (discussed in detail in section 4c) are quite similar to the delayed oscillator theory in which Rossby wave propagation, and the thermocline adjustment to those waves, provides a delayed negative feedback. A positive feedback comes from mid-latitude air-sea feedback and/or from oceanic convective processes involving temperature and salinity.

For the mid-latitude pathway, both diagnostic analyses and sensitivity experiment show that a tripole SST anomaly pattern can produce an anomalous wind stress response over the mid-latitudes. In turn, these winds create a Rossby wave, and the adjustment to that wave tends to amplify the initial central Pacific SST anomaly and therefore is a positive feedback to the central Pacific. This mid-latitude pathway is consistent with observational studies (e.g. Schneider et al. 2002).

The three pathways in the GFDL model appear to exist in observations. We present observational characteristics associated with a very significant phase shift of

the PDO: the 1976/77 North Pacific regime shift. Figs. 18a-c exhibits the time history of observed SST and surface wind stress anomalies along 30^{o}N, 40^{o}N, and 50^{o}N from year 1966 to 1990. In the western subtropics the negative SST anomalies developed in the early 1970s (Fig. 18a), when positive SST anomalies were still present in the KOE region (Fig. 18b). The subtropical cooling signal then gradually extended to the central Pacific in late 1970s, likely advected by the mean current, and remained until the late 1980s. Along with cooling in the subtropics, the surface wind anomalies in the mid-latitude and subtropics switched from easterly to westerly (Fig. 18a, b). Negative SST anomalies were also observed in the western subpolar region in the early 1970s, occurring before the KOE cooling (Fig. 18c versus Fig. 18b). In contrast to the subtropical region, the western subpolar cooling anomaly appears to propagate from the east. This is not surprising, since the mean current in this region flows westward, while the mean current in the subtropical region is eastward. As shown in Fig. 18b, the mid-latitude SST cooled first in the central Pacific around 1975, which was accompanied by a strong westerly wind anomaly. The cooling anomaly further amplified and expanded westward. After 5 years (in the early 1980s), negative SST anomalies emerged in the latitude of the KOE east of Japan and persisted through 1989.

The time history of SST and wind stress anomalies at different latitudes suggests that the negative SST anomalies over the western subtropical, western subpolar and central Pacific Oceans led the KOE SST cooling during the 1976/1977 regime shift. This implies that the KOE SST anomaly is likely a delayed response to the subtropical,

subpolar and central Pacific anomalies. Significant roles of temperature anomalies over the western subtropical and subpolar regions in the PDO phase shift can also be seen from the SST evolution along 165^{o}E (Fig. 18d). Fig. 18d shows that cold anomalies first emerged in the subpolar/subtropical regions around the early 1970s. They then propagated southward/northward to the KOE region and possibly initiated the regime shift of the PDO in the 1976/1977.

The mid-latitude SST feedback to the atmosphere and the relative importance of the three pathways will be the subject of future work. Our study here attempts to highlight the role of local ocean-atmosphere interaction in causing the PDO decadal peak, but does not completely exclude the influence of the tropical Pacific and stochastic noise from atmospheric internal variability. It is worth noting that the mechanism of the PDO proposed in the present paper may be model dependent. The three pathways suggested here seem to exist in observations (Fig. 18), but it is still very difficult to verify these processes due to lack of observational data. This highlights the need for continued and enhanced observations, particularly in the subsurface ocean.

Acknowledgements

The authors would like to thank two anonymous reviewers who provided very valuable feedback and constructive comments that led to substantial improvements in the manuscript. We also thank Dr. Anthony Rosati, Dr. Liang Zhi, Dr. Balaji Venkatramani, Dr. Fanrong Zeng and Dr. Michael Winton for their great help in code

1 modification for the partial coupling sensitivity experiments. We would also like to
2 thank Dr. Young-Oh Kwon for helpful discussions and suggestions.
3

Reference

Allan, R., and T. Ansell, 2006: A New Globally Complete Monthly Historical Gridded Mean Sea Level Pressure Dataset (HadSLP2): 1850–2004. *J. Climate*, **19**, 5816–5842.

Biondi, F., A. Gershunov and D. R. Cayan, 2001: North Pacific decadal climate variability since 1961. *J. Climate*, **14**, 5-10.

Cayan, D. R., S. A. Kammerdiener, M. D. Dettinger, J. M. Caprio, and D. H. Peterson, 2001: Changes in the onset of spring in the western United States. *Bull. Amer. Meteor. Soc.*, **82**, 399-415.

Compo, G. P., J. S. Whitaker, P. D. Sardeshmukh, N. Matsui, B. J. Allan, X. Yin, B. E. Gleason, R. S. Vose, and G. Rutledge, 2011: The twentieth century reanalysis project. *Quarterly. J. Roy. Meteorol. Soc.*, **137**, 1–28.

Deser, C., A. S. Phillips, and J. W. Hurrell, 2004: Pacific interdecadal climate variability: linkages between the tropics and the North Pacific during boreal winter since 1900. *J. Climate*, **15**, 3109-3124.

Deser, C., M. A. Alexander, and M. S. Timlin, 1996: Upper-ocean thermal variations in the North Pacific during 1970-1991. *J. Climate*, **9**, 1840-1855.

Deser, C., and M. L. Blackmon, 1995: On the relationship between tropical and North Pacific sea surface temperature variations. *J. Climate*, **8**, 1677–1680.

d'Orgeville, M. D., and W. R. Peltier, 2009: Implications of both statistical equilibrium and global warming simulations with CCSM3. Part I: on the decadal

variability in the North Pacific basin. *J. Climate*, **22**, 5277-5297.

Delworth, T. L., and Coauthors, 2006: GFDL's CM2 Global Coupled Climate Models. Part I: Formulation and Simulation Characteristics. *J. Climate*, **19**, 643–674.

Delworth, T. L., and Coauthors, 2012: Simulated Climate and Climate Change in the GFDL CM2.5 High-Resolution Coupled Climate Model. *J. Climate*, **25**, 2755–2781.

Donner, L. J., and Coauthors, 2011: The Dynamical Core, Physical Parameterizations, and Basic Simulation Characteristics of the Atmospheric Component AM3 of the GFDL Global Coupled Model CM3. *J. Climate*, 24, 3484–3519.

Frankignoul, C., and N. Sennéchael, 2007: Observed Influence of North Pacific SST Anomalies on the Atmospheric Circulation. *J. Climate*, **20**, 592–606.

Gedalof, Z., N. J. Mantua, and D. L. Peterson, 2002: A multi-century perspective of variability in the Pacific decadal oscillation: new insights from tree rings and coral. *Geophys. Res. Lett.*, **29**, doi:10.1029/2002GL015824.

Gu, D., and S. G. H. Philander, 1997: Interdecadal climate fluctuations that depend on exchange between the tropics and extratropics. *Science*, **275**, 805–807.

Horel, J. D., and J. M. Wallace, 1981: Planetary-scale atmospheric phenomena associated with the Southern Oscillation. *Mon Wea. Rev.*, **109**, 813–829.

Jin, F. F., 1997: A theory of interdecadal climate variability of the North Pacific ocean–atmosphere system. *J. Climate*, **10**, 1821–1835.

Kelly, K., and S. Dong, 2004: The relationship of western boundary current heat transport and storage to midlatitude ocean–atmosphere interaction. Earth Climate:

The Coupled Ocean–Atmosphere Interaction. *Geophys. Monogr.*, **147**, 347–364.

Kushnir, Y., W. A. Robinson, I. Bladé, N. M. J. Hall, S. Peng, and R. Sutton, 2002: Atmospheric GCM response to extratropical SST anomalies: Synthesis and evaluation. *J. Climate*, **15**, 2233-2256.

Kwon, Y-O., and C. Deser, 2007: North Pacific decadal variability in the community climate system model version 2. *J. Climate*, **20**, 2416-2433.

Latif, M., and T. P. Barnett, 1994: Causes of decadal climate variability over the North Pacific and North America. *Science*, **266**, 634-637.

Latif, M., and T. P. Barnett, 1996: Decadal climate variability over the North Pacific and North America: Dynamics and predictability. *J. Climate*, **9**, 2407-2423.

Liu, Z., 2012: Dynamics of interdecadal climate variability: a historical perspective. *J. Climate*, **25**, 1963-1995.

Mantua, N. J., S. R. Hare, Y. Zhang, J. M. Wallace, and R. C. Francis, 1997: A Pacific interdecadal climate oscillation with impacts on salmon production. *Bull. Amer. Meteor. Soc.*, **78**, 1069-1079.

Mann, M. E., and J. Lees, 1996: Robust Estimation of Background Noise and Signal Detection in Climatic Time Series. Climatic Change, 33, 409-445.

Miller, A. J., D. R. Cayan, T. P. Barnett, N. E. Graham, and J. M. Oberhuber, 1994: Interdecadal variability of the Pacific Ocean: model response to observed heat flux and wind stress anomalies. *Climate Dyn.*, **9**, 287-302.

Minobe, S., 1997: A 50-70 year climate oscillation over the North Pacific and North America. *Geophys. Res. Lett.*, **24**,683-686.

Nakamura, H., G. Lin, and T. Yamagata, 1997: Decadal climate variability in the North Pacific during the recent decades. *Bull. Amer. Meteor. Soc.*, **78**, 2215-2225.

Newman, M., G. P. Compo, and M. A. Alexander, 2003: ENSO forced variability of the Pacific decadal oscillation. *J. Climate*, **16**, 3853–3857.

Pierce, D., T. Barnett, N. Schneider, R. Saravanan, D. Dommenget, and M. Latif, 2001: The role of ocean dynamics in producing decadal climate variability in the North Pacific. *Climate Dyn.*, **18**, 51–70.

Qiu, B., S. Chen, N. Schneider, and B. Taguchi, 2014: A coupled decadal prediction of the dynamic state of the Kuroshio Extension system. *J. Climate*, **27**, 1751-1764.

Schneider, N., A. J. Miller, M. A. Alexander, and C. Deser, 1999: Subduction of decadal North Pacific temperature anomalies: observations and dynamics. *J. Phys. Oceanogr.*, **29**, 1056-1070.

Schneider, N., A. J. M iller, and D. W. Pierce, 2002: Anatomy of North Pacific decadal variability. *J. Climate*, **15**, 586–605.

Seager, R., Y. Kushnir, N. H. Naik, M. A. Cane, and J. Miller, 2001: Wind-driven shifts in the latitude of the Kuroshio–Oyashio Extension and generation of SST anomalies on decadal timescales. *J. Climate*, **14**, 4249–4265.

Smith, T.M., and R.W. Reynolds, 2004: Improved extended reconstruction of SST. *J. Climate*, **17**, 2466-2477.

Vecchi, G.A., and Coauthors, 2014: On the Seasonal Forecasting to Regional Tropical Cyclone Activity. Submitted to *J. Climate*.

Wijffels, S., E. Firing, and H. Bryden, 1994: Direct Observations of the Ekman Balance at 10 ºN in the Pacific. *J. Phys. Oceanogr.*, **24**, 1666–1679.

Wu, L., Z. Liu, A. R. Ga llimore, R. Jacob, D. Lee, and Y. Zhong, 2003: Pacific decadal variability: the tropical Pacific mode and the North Pacific mode. *J. Climate*, **16**, 1101-1120.

Wu, L., E. L. Dong, and Z. Liu, 2005: The 1976/77 North Pacific Climate Regime Shift: The Role of Subtropical Ocean Adjustment and Coupled Ocean–Atmosphere Feedbacks*. *J. Climate*, **18**, 5125–5140.

Xie, S.-P., T. Kunitani, A. Kubokawa, M. Nonaka, and S. Hosoda, 2000: Interdecadal thermocline variability in the North Pacific for 1958–97: A GCM simulation. *J. Phys. Oceanogr.*, **30**, 2798–2813.

Zhong, Y., Z. Liu, and R. Jacob, 2008: Origin of Pacific multidecadal variability in community climate system model version 3 (CCSM3): a combined statistical and dynamical assessment. *J. Climate*, **21**, 114-133.

Zhong, Y., and Z. Liu, 2009: On the mechanism of Pacific multidecadal climate variability in CCSM3: the role of the subpolar North Pacific Ocean. *J. Climate*, **39**, 2052-2076.

Table list:

Table 1: The six models developed at GFDL involved in this study and their resolution, parameterization scheme, and reference.

Figure Captions:

Figure 1: Shown are the PDO behaviors in observations. (a-b) Regression of SST (^{o}C) and surface wind stress (N/m^{2}) against the (c) PDO index which is defined as the principal component time series of leading EOF over the North Pacific Ocean (20^{o}-60^{o}N). (a) represents the PDO warm phase and (b) represents the PDO cold phase. The principal component time series (c) is normalized by its standard deviation, thus the amplitudes in (a) and (b) correspond to one standard deviation change of the corresponding principal component time series. The SST is from ERSST datasets (Smith and Reynolds 2003), while the surface wind stress is from 20CRv2 (Compo et al. 2012).

Figure 2: Same as Fig. 1a but for different versions of GFDL coupled model (a) CM2.1, (b) CM2.5_FLOR, (c) CM2.5_FLOR_FA, (d) CM2.5, (e) CM2.6 and (f) CM3.

Figure 3: Multitaper spectrum (Mann and Lees 1996) of the normalized annually PDO index in different versions of GFDL coupled model (a) CM2.1, (b) CM2.5_FLOR, (c) CM2.5_FLOR_FA, (d) CM2.5, (e) CM2.6 and (f) CM3. We use three tapers in all spectrum analysis in this study. Note that using more tapers will not change the conclusion, although the resolution of the spectrum is reduced.

Figure 4: Shown are the PDO behaviors in stochastic (a-c) and TPAC_RESTORE (without ENSO forcing, d-f) runs. (a) Regression of SST against the normalized KOE SST index which is multiplied by -1. Unit is ^{o}C. (b) Power spectrum of the normalized KOE SST index. (c) Zonal

mean standard deviation of annual mean Pacific SST in the fully coupled control run (red line) and stochastic run (blue line). Unit is ^{o}C. (d-f) are the same as (a-c) but for the TPAC_RESTORE run.

Figure 5: (a) Regression of SLP (hPa) against the normalized KOE SST index (multiple by -1) in the fully coupled control run. (b) Power spectrum of the North Pacific Index in control run. (c-d) are the same as (a-b) but for stochastic run. (e-f) are the same as (a-b) but for the CM2.5_FLOR run.

Figure 6: Lagged regression of SST (shading in left panel, ^{o}C), and surface net heat flux (contours in left panel, black (white) contours imply heating (cooling) the ocean, W/m^{2}), surface wind stress (vector in right panel, N/m^{2}) and wind stress curl (shading in right panel, 10^{-8} N/m^{3}) against the PDO index in CM2.5_FLOR model. All data are 10-30-yr band-pass filtered before regression. The gray contours in the right panel denote the long term mean zero wind stress curl lines. The yellow boxes in (a) denote the regions for heat budget analysis in Fig. 9.

Figure 7: Lagged regression of zonal mean (west coast to 180^{o}E) temperature (left panel, ^{o}C), salinity (middle panel, psu) and zonal velocity (shading in the right panel, cm/s) on the PDO index in CM2.5_FLOR model. All data are 10-30-yr band-pass filtered before regression. Contours in (a) denotes the long term mean vertical velocity (solid/dash lines mean upward/downward movements) and the contour interval is 1×10^{-6} m/s. Black contours overlapped on the right panel indicate the long term mean zonal velocity fields, which can represent the subtropical and subpolar gyre boundary.

Figure 8: Lagged regression of (a) temperature (^{o}C) and (b) salinity (psu) in the surface of the KOE region (blue, 35^{o}-45^{o}N, 140^{o}-180^{o}E, 0-50m), surface of the subpolar region (red, 48^{o}-54^{o}N, 160^{o}-180^{o}E, 0-100m) and subsurface of the subpolar region (green, 48^{o}-54^{o}N, 160^{o}-180^{o}E,

150-350m) against the PDO index in CM2.5_FLOR model. (c) is the same as (a) but for the surface KOE region, surface subtropical region (red, 25°-30°N, 140°-170°E, 0-50m) and subsurface subtropical region (green, 25°-30°N, 140°-170°E, 100-300m). All data are 10-30-yr band-pass filtered before regression.

Figure 9: Lagged regression of different heat budget terms averaged over the (a) KOE region (35°-45°N, 140°-170°E), (b) central Pacific Ocean (25°-42°N, 180°-150°W) and (c) northeastern Pacific Ocean (45°-57°N, 156°-125°W) against the PDO index in the CM2.5_FLOR model. All data are 10-30-yr band-pass filtered before regression. Units are W/m^2 for heat budget term and °C for SST. Blue curve with circles denotes surface net heat flux (positive downward), green curve with cross signs denotes total zonal temperature advection, magenta curve with squares denotes total meridional temperature advection, yellow curve denotes total vertical temperature advection, back curve with diamonds denotes residual (includes horizontal, vertical diffusions, convection and vertical entrainment), dash blue curve denotes temperature advection by the anomalous meridional current, dash grey curve denotes temperature advection by the anomalous meridional Ekman current, dash green curve denotes temperature advection by the anomalous meridional geostrophic current, and red curve with asterisks denotes SST.

Figure 10: Schematic picture of the PDO full cycle. This diagram is based on Zhong and Liu (2009), and modified to show mechanisms operating in the GFDL models.

Figure 11: North Pacific air-sea feedback in CM2.5_FLOR model. Seasonal evolution of lead-lag regression between the KOE SST index (defined as the area averaged SST anomalies in 35°-45°N, 140°-180°E) and geopotential height anomalies over the Aleutian low region (30°-60°N, 150°-150°W) for (a) 850mb and (b) 250mb (Shaded area exceeds 95% confidence level based on

an F test). Ordinate indicates the calendar month taken for the KOE index lead-lag regressed against the time series of geopotential height anomalies for a particular lag indicated on the abscissa. Unit is m/^{o}C. (c) Lagged regression of wind stress and wind stress curl (shading) on the normalized KOE index with wind stress (curl) leading KOE SST index by 5 years. (d) Same as (c) but with the KOE SST index leading wind stress (curl) by 1 year. Units are N/m^{2} for wind stress and 10^{-8} N/m^{3} for wind stress curl. All variables are 10-30-yr band-pass filtered before regression for (c) and unfiltered for (d). The unfiltered regression pattern is further scaled by the ratio of the standard deviation of 10-30-yr band-pass filtered SST index to that of unfiltered SST index. The gray contours in (c-d) denote the long term mean zero wind stress curl lines. The influence of ENSO is filtered out by using a linear regression onto the Niño3 index.

Figure 12: (a) Annual mean SLP (hPa), (b) wind stress (N/m^{2}) and wind stress curl (10^{-8} N/m^{3}) responses to the SST anomaly north of 20^{o}N during the mature cold phase of PDO (Fig. 6g). (c) and (d) are the same as (a) and (b) but with the tripole SST forcing (Fig. 6d) over the North Pacific Ocean. The black points overlapped on the shading indicate that at least 80% ensemble members have the same sign as the ensemble mean.

Figure 13: Lead-lag correlation between the annually (a) subsurface subpolar (48^{o}-54^{o}N, 160^{o}-180^{o}E, 150-350m) temperature and the PDO index in CM2.5_FLOR model. (b) Same as (a) but for the subsurface subtropical (25^{o}-30^{o}N, 140^{o}-170^{o}E, 100-300m) temperature. All data are 10-30-yr band-pass filtered before correlation. Positive (negative) values in x-axis indicate PDO leads (lags). The black point overlapped on the bold solid line denotes that the correlation is significant at 5% significance level based on the Monte-Carlo test.

Figure 14: Time evolution of SST (left panel) and zonal mean (140^{o}-180^{o}E) temperature (right panel) anomalies in response to imposing a constant wind stress pattern corresponding to the PDO warm phase. Unit is ^{o}C.

Figure 15: The averaged first baroclinic Rossby wave speed over the North Pacific Ocean (cm/s) and the corresponding basin-crossing time (year) in CM2.5_FLOR model.

Figure 16: Regression of warm season (AMJJAS) precipitation (shading, Unit is mm/day) and sea level pressure (contours, Unit is hPa) against the normalized unfiltered PDO index in (a) CM2.5_FLOR model and (b) observation. The influence of ENSO is filtered out by using a linear regression onto the Niño3 index. The precipitation data is from Climatic Research Unit (CRU) high resolution (0.5×0.5 degree) precipitation time-series dataset and SLP data is from Met Office Hadley Center's sea level pressure HadSLP2.

Figure 17: Same as Fig. 16 but for the cold season (ONDJFM).

Figure 18: Shown are the 1976/1977 climate regime shifts over the North Pacific Ocean in observations. SST (shading, ^{o}C) and wind stress (vectors, N/m^{2}) anomalies along (a) 30^{o}N, (b) 40^{o}N and (c) 50^{o}N in the Pacific. (d) Hovmöller diagram of SST anomaly (^{o}C) evolution along 165^{o}E. All data are 10-yr low pass filtered.

Table 1: The six models developed at GFDL involved in this study and their resolution, parameterization scheme, and reference

Model	**Ocean Horizontal Resolution**	**Ocean: Use of mesoscale eddy parameterization**	**Use of Flux Adjustments**	**Atmosphere: Horizontal resolution**	**Atmosphere: # of vertical levels**	**Atmosphere: Chemistry and aerosol indirect effect**	**Reference**
CM2.1	1^o (0.3^o in Tropics)	Yes	No	2^o	24	No	Delworth et al (2006)
CM2.5_FLOR	1^o (0.3^o in Tropics)	Yes	No	0.5^o	32	No	Vecchi et al (2014)
CM2.5_FLOR_FA	1^o (0.3^o in Tropics)	Yes	Yes	0.5^o	32	No	Vecchi et al (2014)
CM2.5	0.25^o	No	No	0.5^o	32	No	Delworth et al (2012)
CM2.6	0.1^o	No	No	0.5^o	32	No	Delworth et al (2012)
CM3	1^o (0.3^o in Tropics)	Yes	No	2^o	48	Yes	Donner et al (2011)

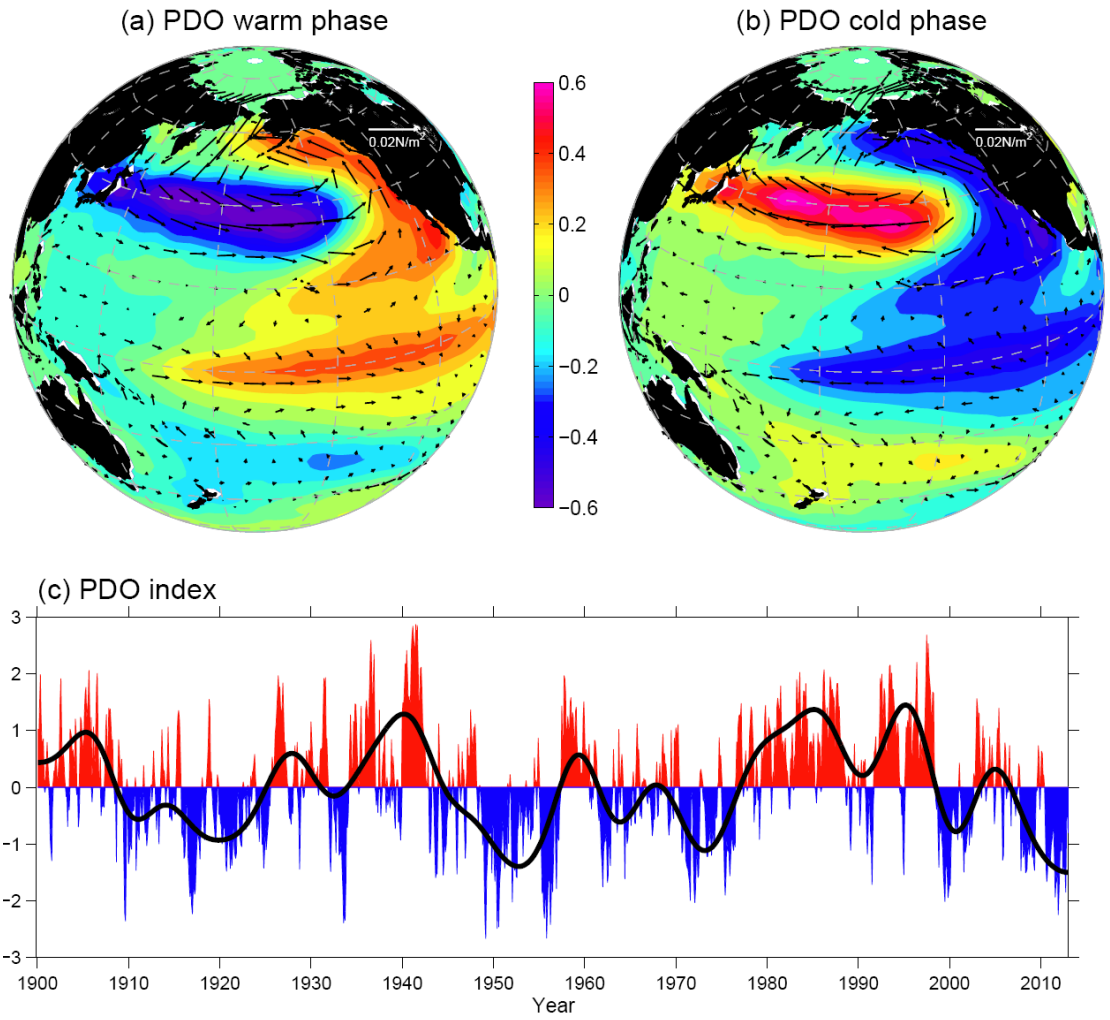

Figure 1: Shown are the PDO behaviors in observations. (a-b) Regression of SST (^{o}C) and surface wind stress (N/m^2) against the (c) PDO index which is defined as the principal component time series of leading EOF over the North Pacific Ocean (20^{o}-60^{o}N). (a) represents the PDO warm phase and (b) represents the PDO cold phase. The principal component time series (c) is normalized by its standard deviation, thus the amplitudes in (a) and (b) correspond to one standard deviation change of the corresponding principal component time series. The SST is from ERSST datasets (Smith and Reynolds 2003), while the surface wind stress is from 20CRv2 (Compo et al. 2012).

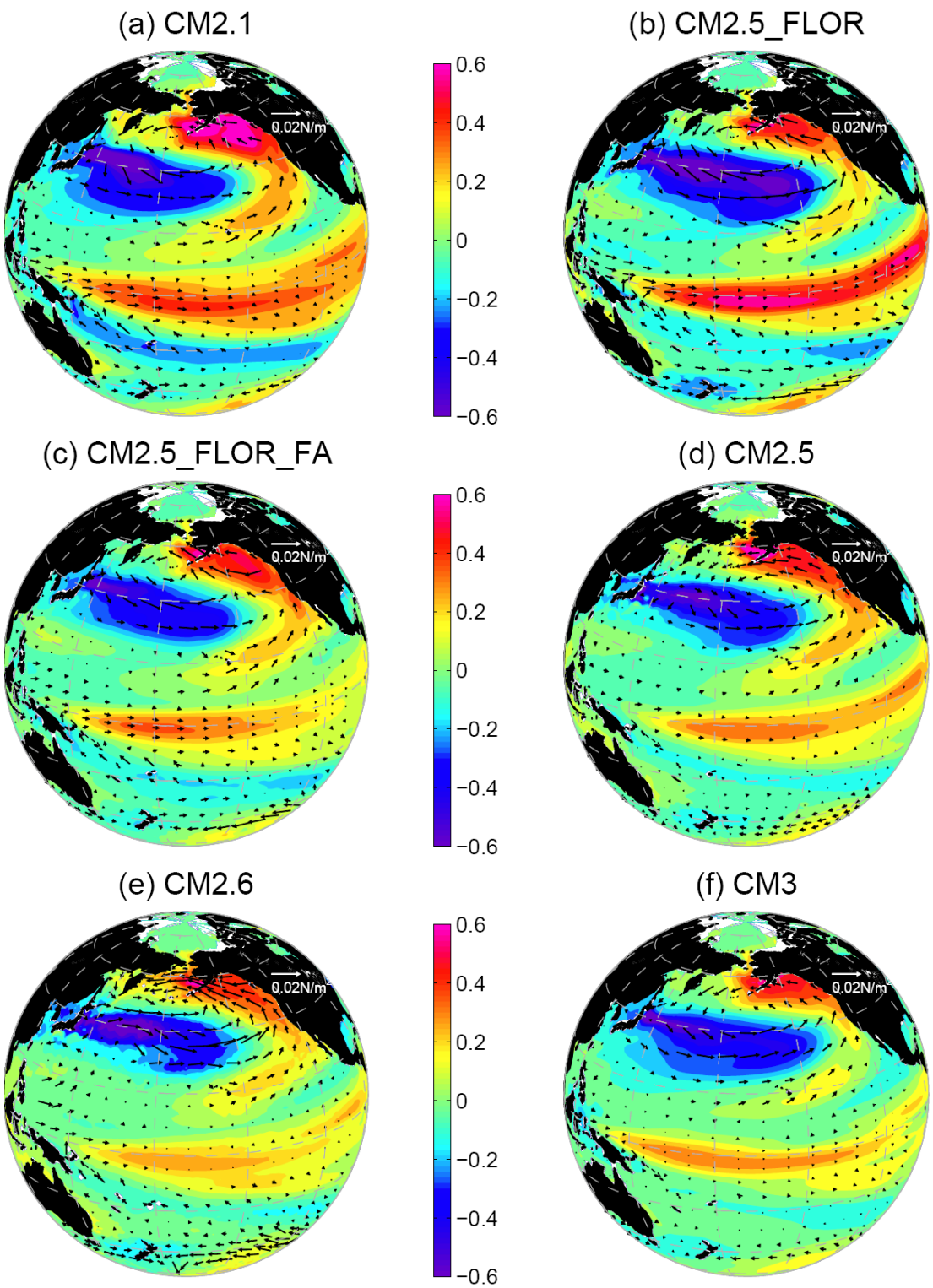

Figure 2: Same as Fig. 1a but for different versions of GFDL coupled model (a) CM2.1, (b) CM2.5_FLOR, (c) CM2.5_FLOR_FA, (d) CM2.5, (e) CM2.6 and (f) CM3.

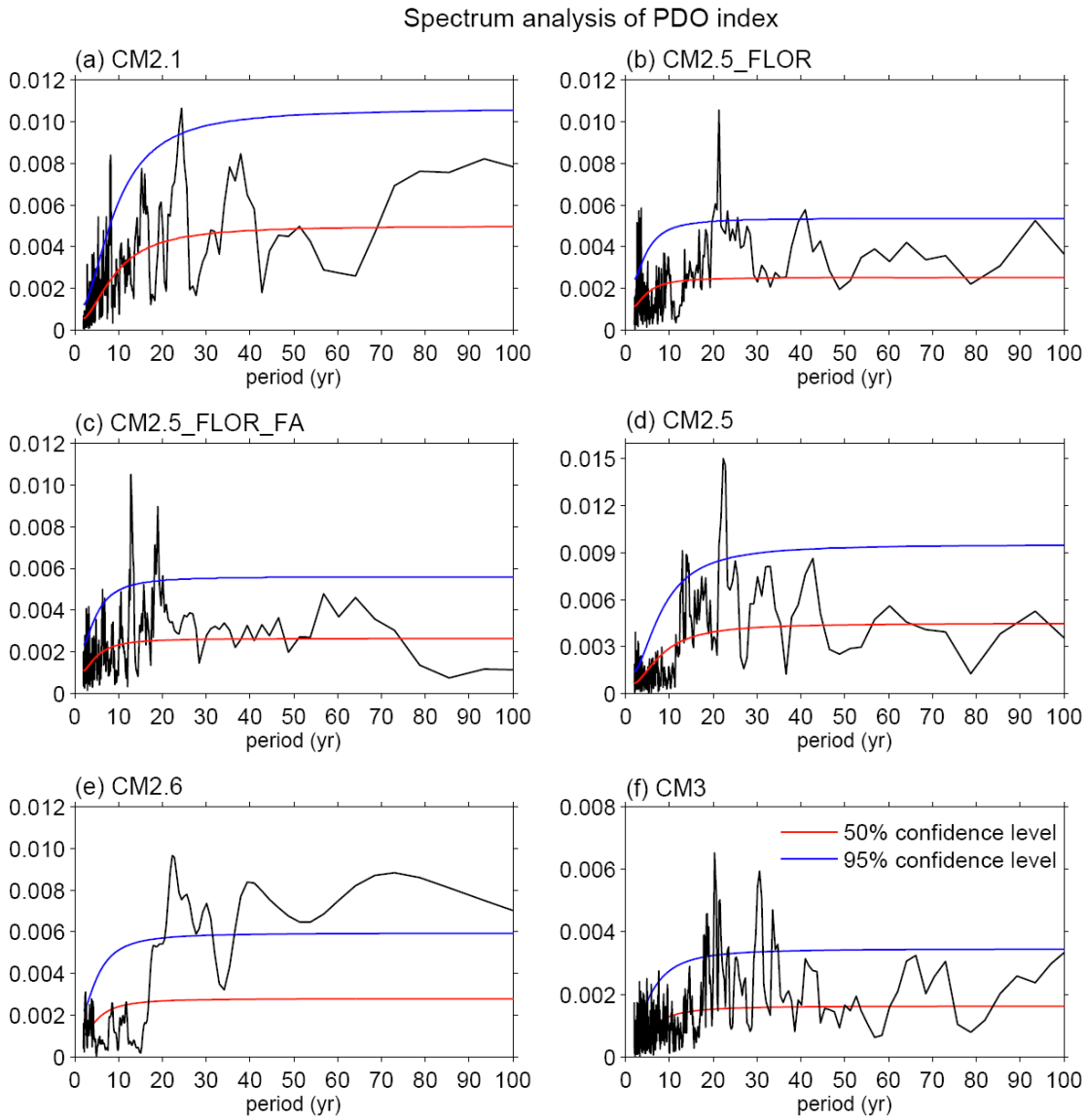

Figure 3: Multitaper spectrum (Mann and Lees 1996) of the normalized annually PDO index in different versions of GFDL coupled model (a) CM2.1, (b) CM2.5_FLOR, (c) CM2.5_FLOR_FA, (d) CM2.5, (e) CM2.6 and (f) CM3. We use three tapers in all spectrum analysis in this study. Note that using more tapers will not change the conclusion, although the resolution of the spectrum is reduced.

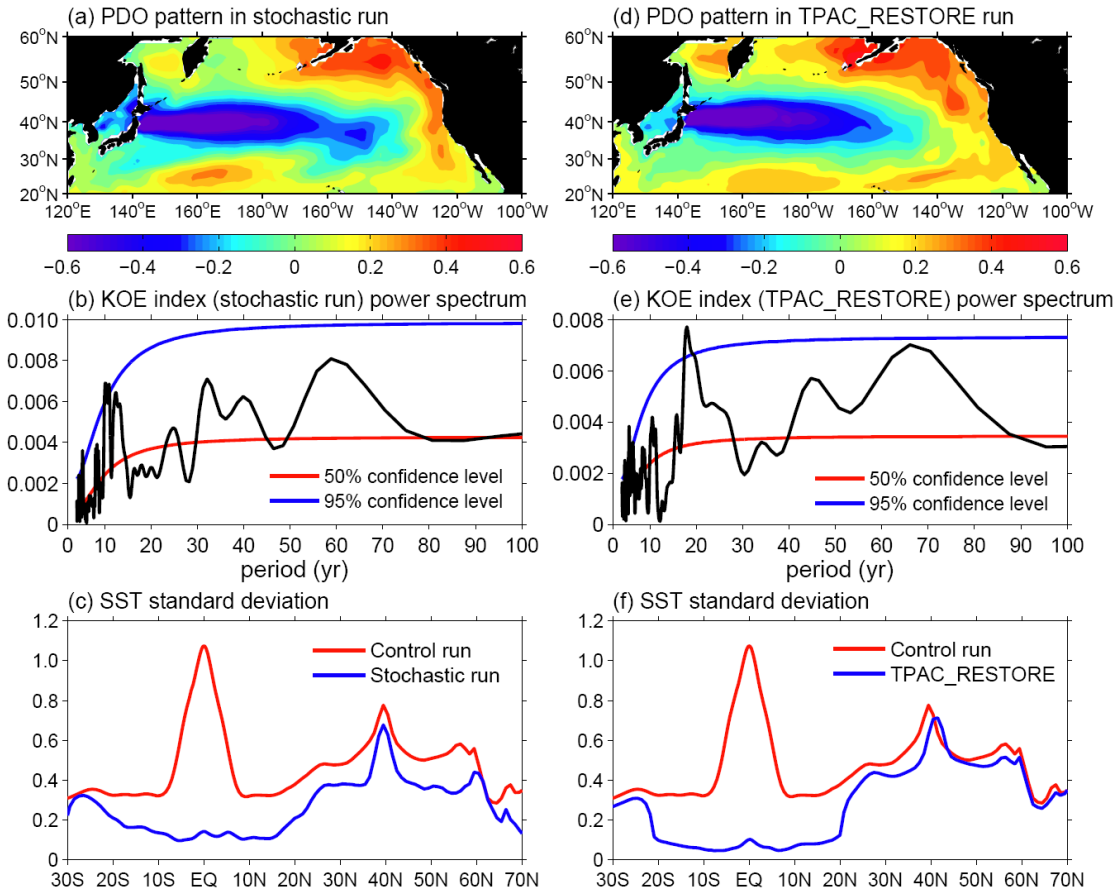

Figure 4: Shown are the PDO behaviors in stochastic (a-c) and TPAC_RESTORE (without ENSO forcing, d-f) runs. (a) Regression of SST against the normalized KOE SST index which is multiplied by -1. Unit is ^{o}C. (b) Power spectrum of the normalized KOE SST index. (c) Zonal mean standard deviation of annual mean Pacific SST in the fully coupled control run (red line) and stochastic run (blue line). Unit is ^{o}C. (d-f) are the same as (a-c) but for the TPAC_RESTORE run.

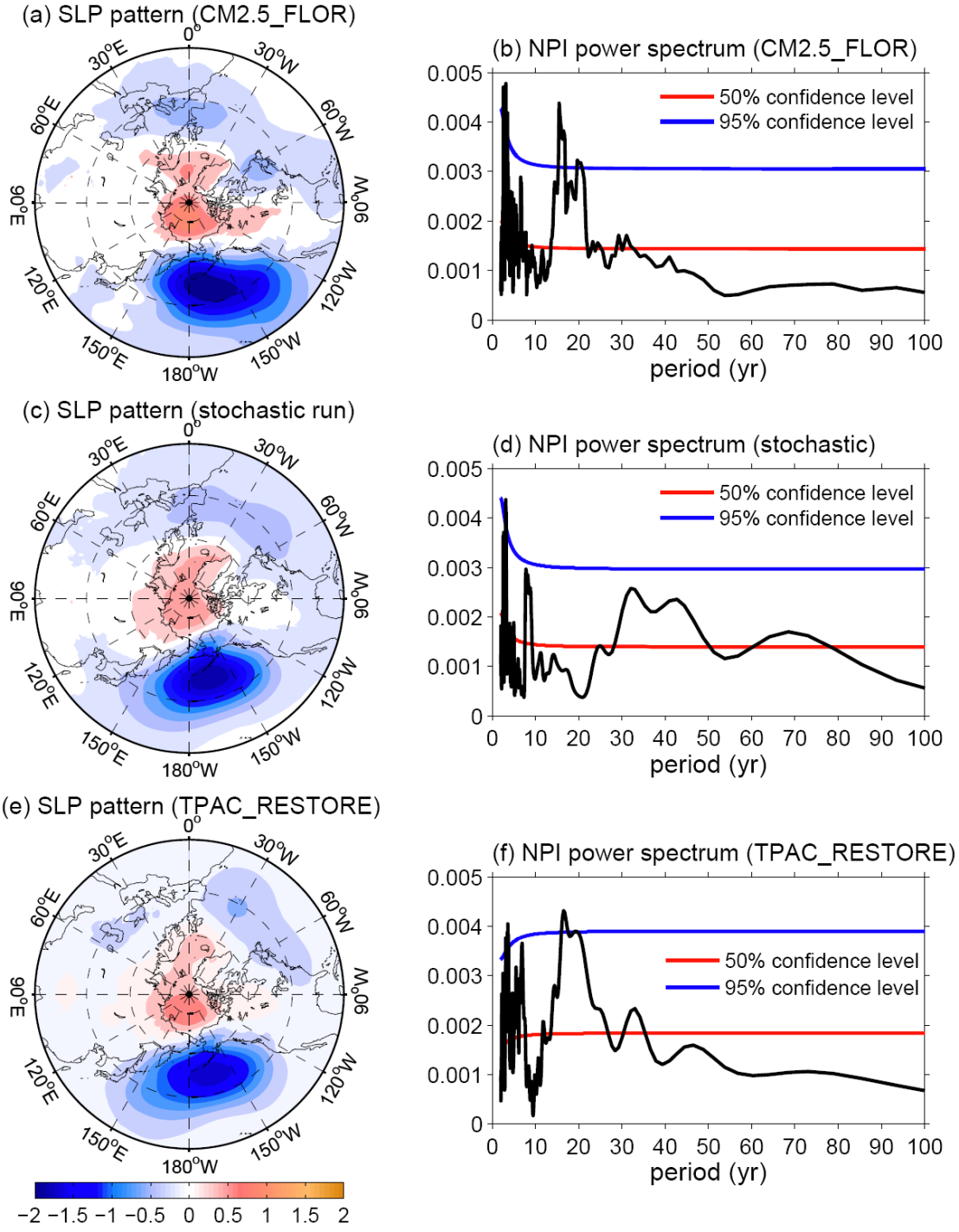

Figure 5: (a) Regression of SLP (hPa) against the normalized KOE SST index (multiple by -1) in the fully coupled control run. (b) Power spectrum of the North Pacific Index in control run. (c-d) are the same as (a-b) but for stochastic run. (e-f) are the same as (a-b) but for the CM2.5_FLOR run.

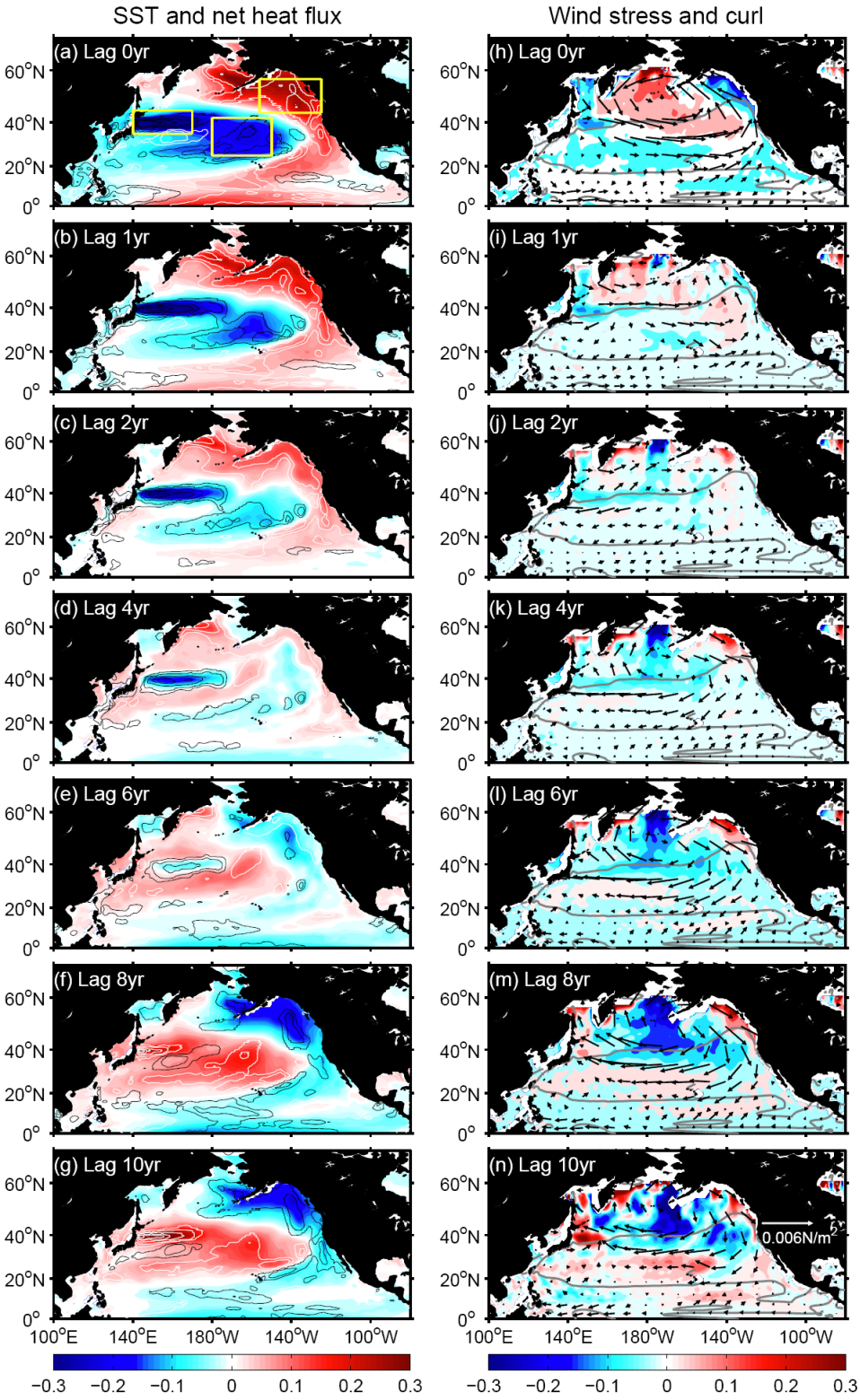

Figure 6: Lagged regression of SST (shading in left panel, ^{o}C), and surface net heat flux (contours in left panel, black (white) contours imply heating (cooling) the ocean, W/m^2), surface wind stress (vector in right panel, N/m^2) and wind stress curl (shading in right panel, 10^{-8} N/m^3) against the PDO index in CM2.5_FLOR model. All data are 10-30-yr band-pass filtered before regression. The gray contours in the right panel denote the long term mean zero wind stress curl lines. The yellow boxes in (a) denote the regions for heat budget analysis in Fig. 9.

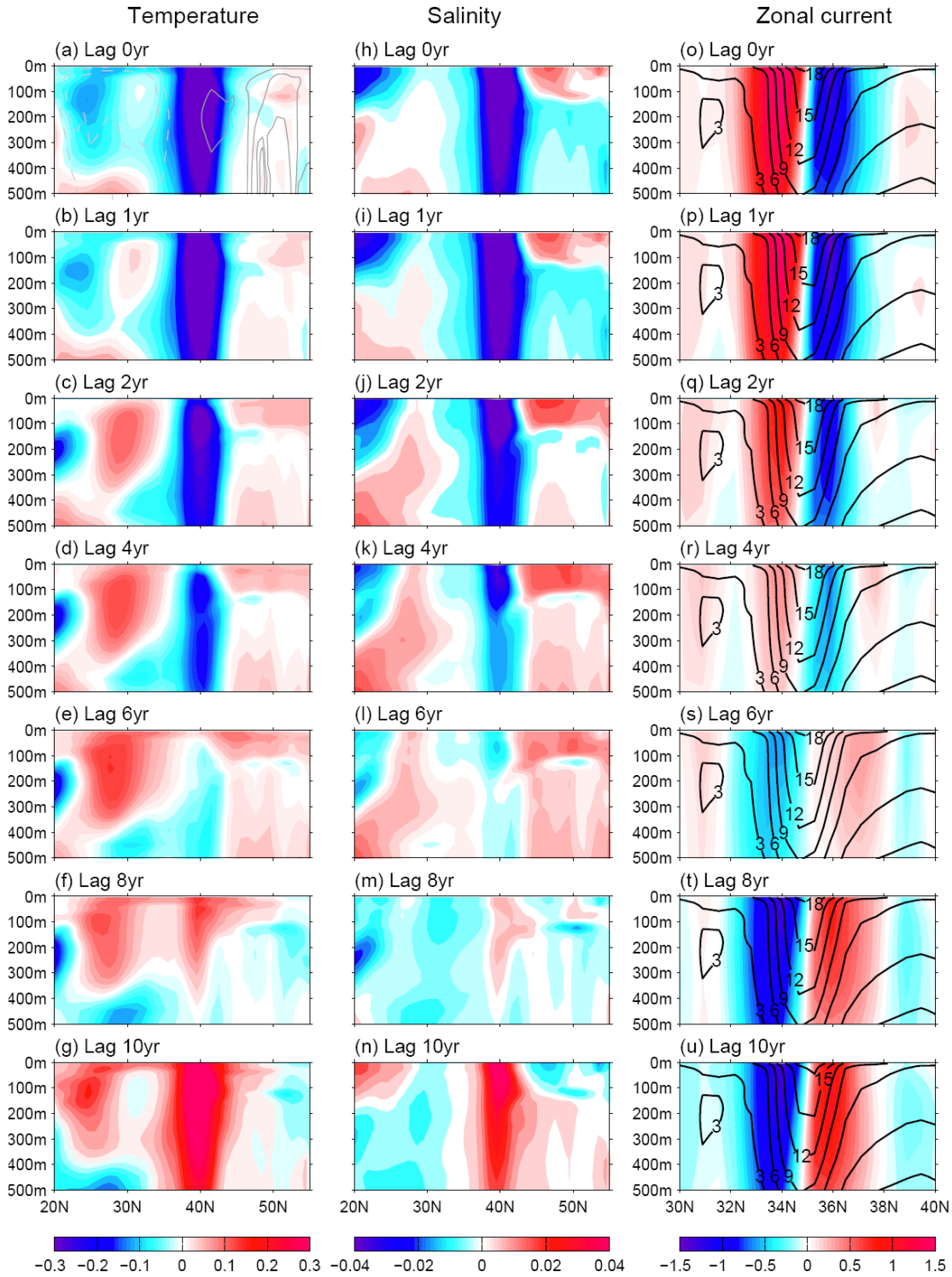

Figure 7: Lagged regression of zonal mean (west coast to 180°E) temperature (left panel, °C), salinity (middle panel, psu) and zonal velocity (shading in the right panel, cm/s) on the PDO index in CM2.5_FLOR model. All data are 10-30-yr band-pass filtered before regression. Contours in (a) denotes the long term mean vertical velocity (solid/ dash contours mean upward/downward movements) and the contour interval is 1×10^{-6} m/s. Black contours overlapped on the right panel indicate the long term mean zonal velocity fields, which can represent the subtropical and subpolar gyre boundary.

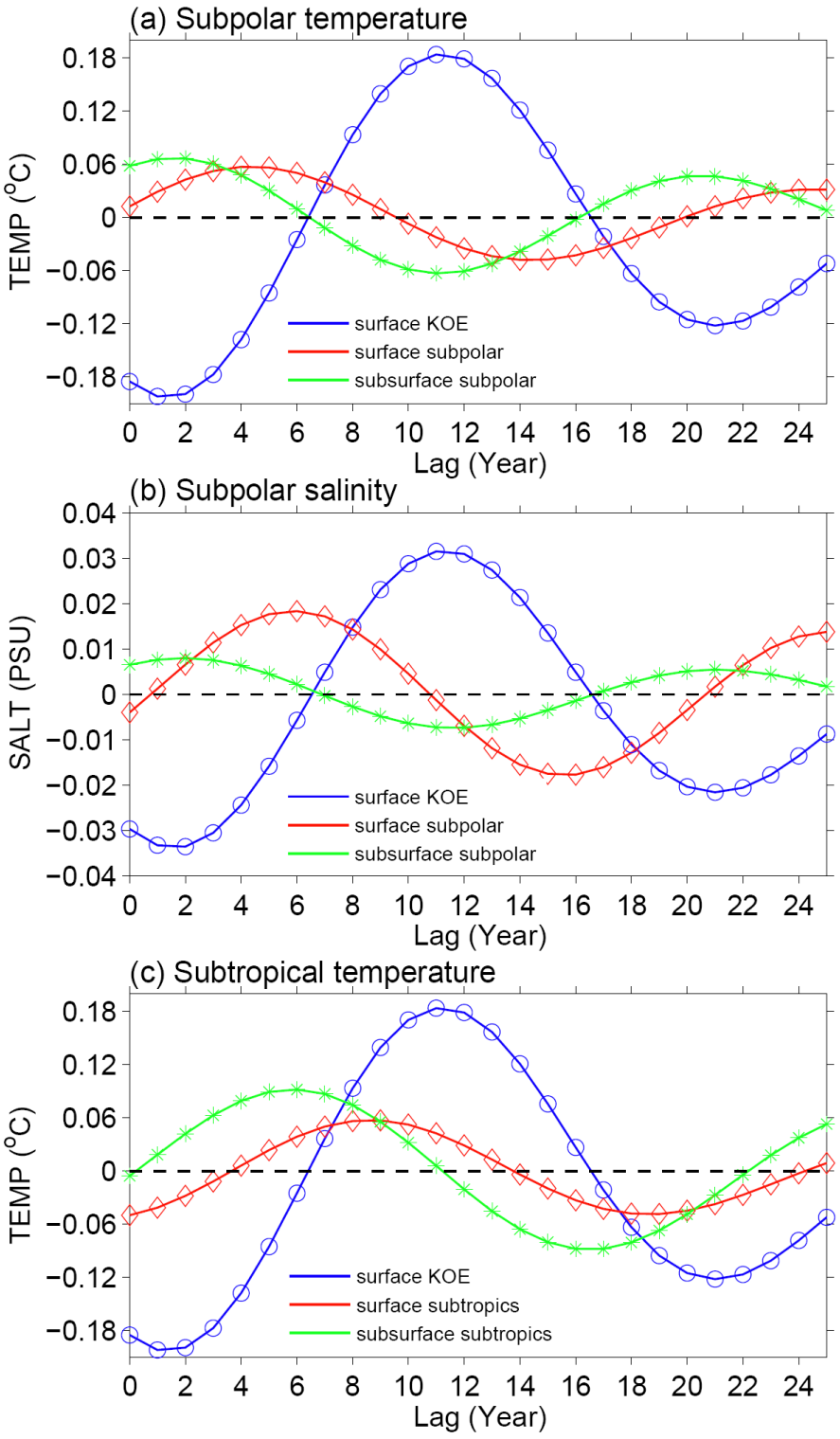

Figure 8: Lagged regression of (a) temperature (°C) and (b) salinity (psu) in the surface of the KOE region (blue, 35°-45°N, 140°-180°E, 0-50m), surface of the subpolar region (red, 48°-54°N, 160°-180°E, 0-100m) and subsurface of the subpolar region (green, 48°-54°N, 160°-180°E, 150-350m) against the PDO index in CM2.5_FLOR model. (c) is the same as (a) but for the surface KOE region, surface subtropical region (red, 25°-30°N, 140°-170°E, 0-50m) and subsurface subtropical region (green, 25°-30°N, 140°-170°E, 100-300m). All data are 10-30-yr band-pass filtered before regression.

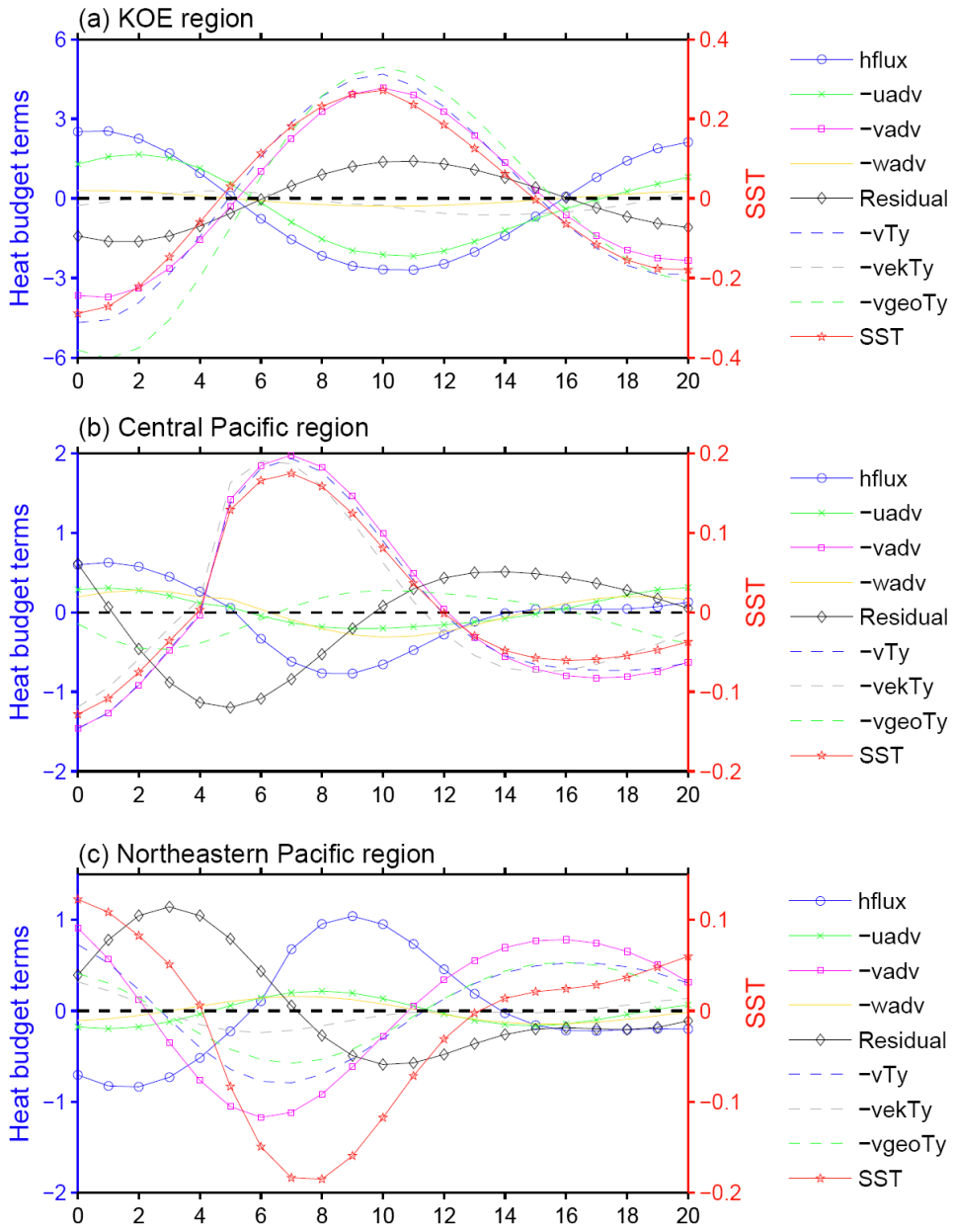

Figure 9: Lagged regression of different heat budget terms averaged over the (a) KOE region (35°-45°N, 140°-170°E), (b) central Pacific Ocean (25°-42°N, 180°-150°W) and (c) northeastern Pacific Ocean (45°-57°N, 156°-125°W) against the PDO index in the CM2.5_FLOR model. All data are 10-30-yr band-pass filtered before regression. Units are W/m^2 for heat budget term and °C for SST. Blue curve with circles denotes surface net heat flux (positive downward), green curve with cross signs denotes total zonal temperature advection, magenta curve with squares denotes total meridional temperature advection, yellow curve denotes total vertical temperature advection, back curve with diamonds denotes residual (includes horizontal, vertical diffusions, convection and vertical entrainment), dash blue curve denotes temperature advection by the anomalous meridional current, dash grey curve denotes temperature advection by the anomalous meridional Ekman current, dash green curve denotes temperature advection by the anomalous meridional geostrophic current, and red curve with asterisks denotes SST.

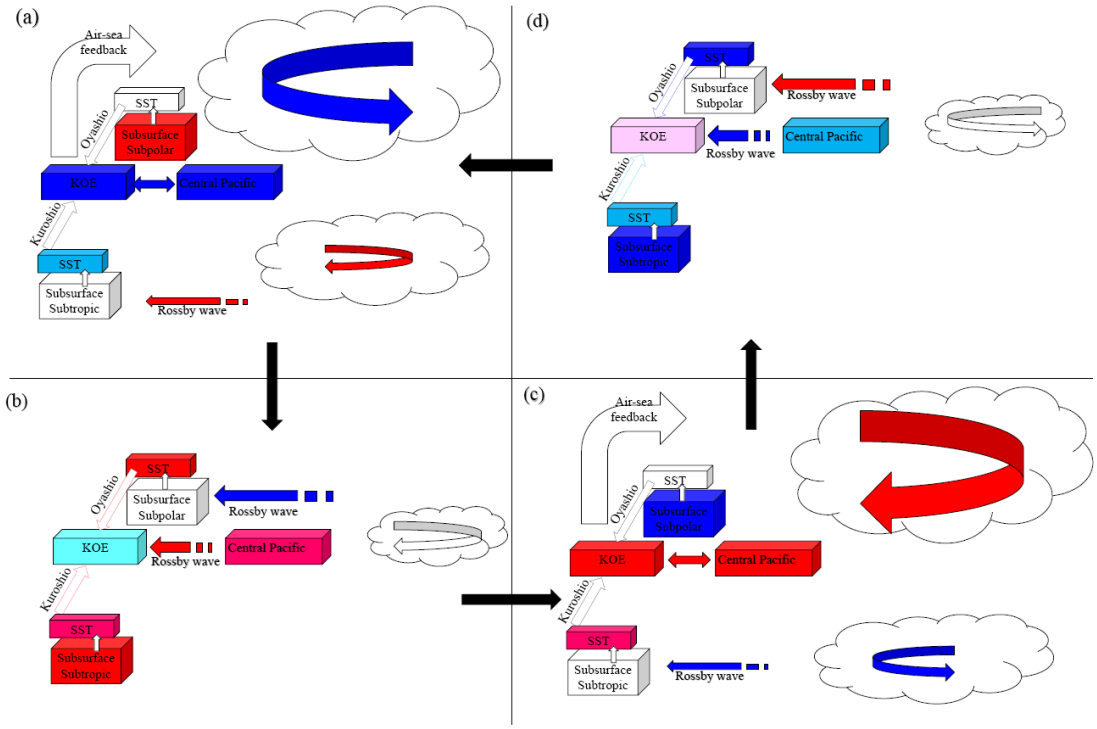

Figure 10: Schematic picture of the PDO full cycle. This diagram is based on Zhong and Liu (2009), and modified to show mechanisms operating in the GFDL models.

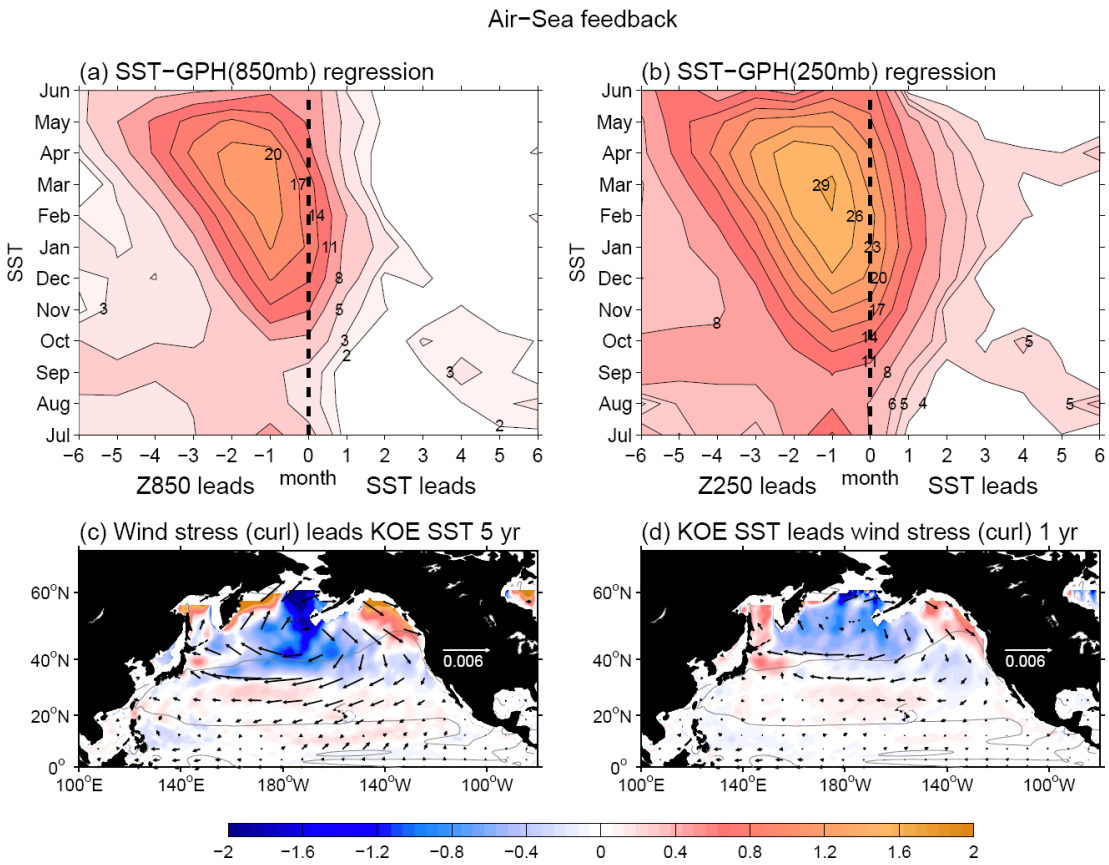

Figure 11: North Pacific air-sea feedback in CM2.5_FLOR model. Seasonal evolution of lead-lag regression between the KOE SST index (defined as the area averaged SST anomalies in 35°-45°N, 140°-180°E) and geopotential height anomalies over the Aleutian low region (30°-60°N, 150°-150°W) for (a) 850mb and (b) 250mb (Shaded area exceeds 95% confidence level based on an F test). Ordinate indicates the calendar month taken for the KOE index lead-lag regressed against the time series of geopotential height anomalies for a particular lag indicated on the abscissa. Unit is m/°C. (c) Lagged regression of wind stress and wind stress curl (shading) on the normalized KOE index with wind stress (curl) leading KOE SST index by 5 years. (d) Same as (c) but with the KOE SST index leading wind stress (curl) by 1 year. Units are N/m^2 for wind stress and 10^{-8} N/m^3 for wind stress curl. All variables are 10-30-yr band-pass filtered before regression for (c) and unfiltered for (d). The unfiltered regression pattern is further scaled by the ratio of the standard deviation of 10-30-yr band-pass filtered SST index to that of unfiltered SST index. The gray contours in (c-d) denote the long term mean zero wind stress curl lines. The influence of ENSO is filtered out by using a linear regression onto the Niño3 index.

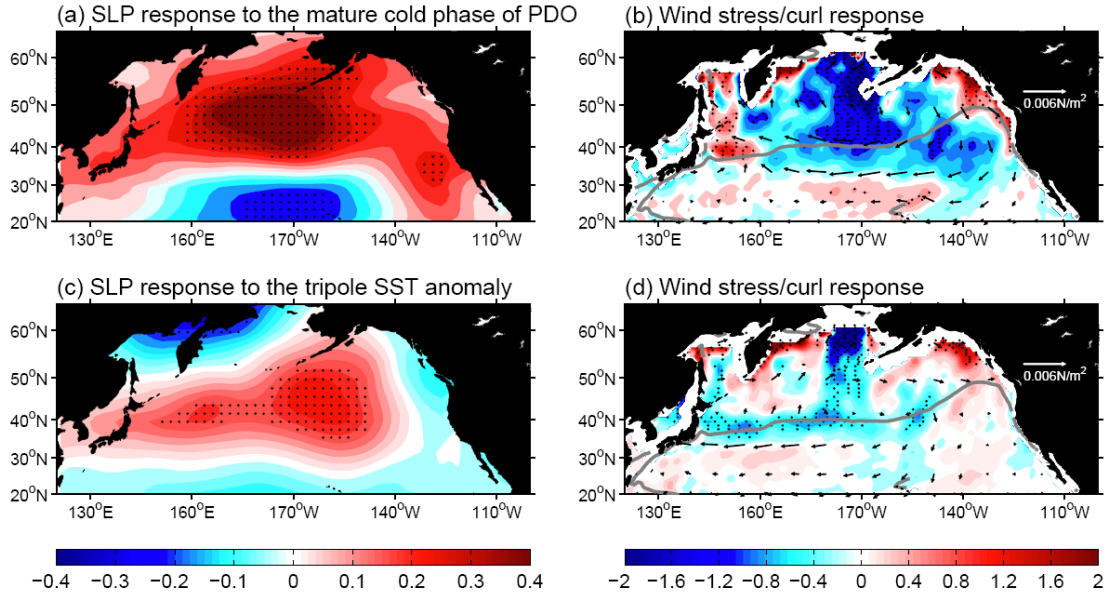

Figure 12: (a) Annual mean SLP (hPa), (b) wind stress (N/m^2) and wind stress curl (10^{-8} N/m^3) responses to the SST anomaly north of 20°N during the mature cold phase of PDO (Fig. 6g). (c) and (d) are the same as (a) and (b) but with the tripole SST forcing (Fig. 6d) over the North Pacific Ocean. The black points overlapped on the shading indicate that at least 80% ensemble members have the same sign as the ensemble mean.

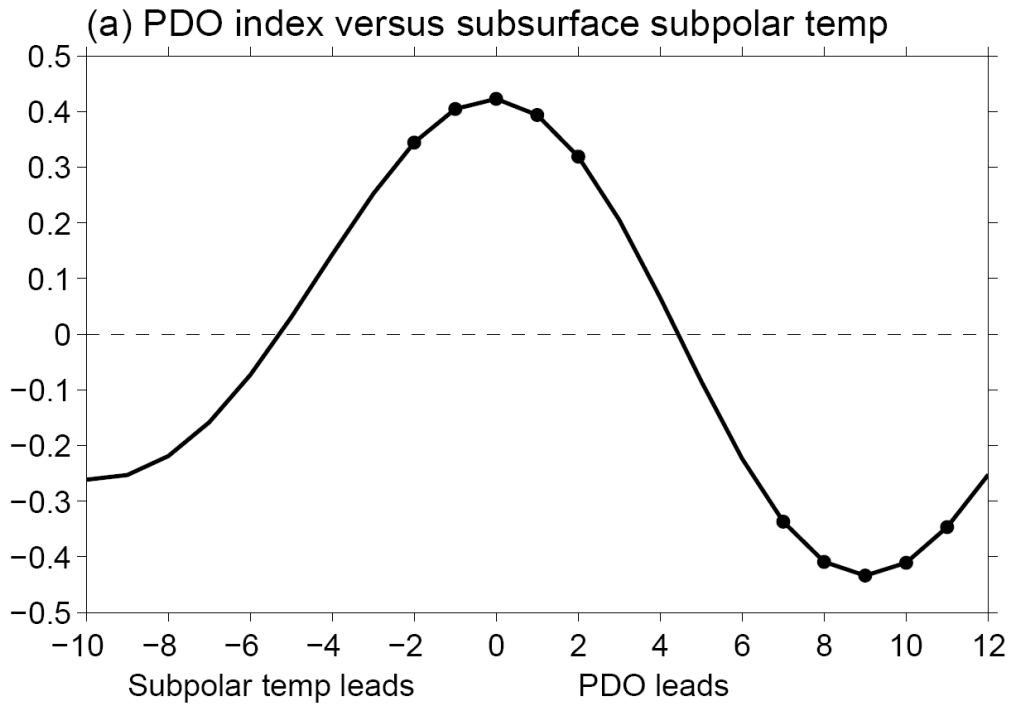

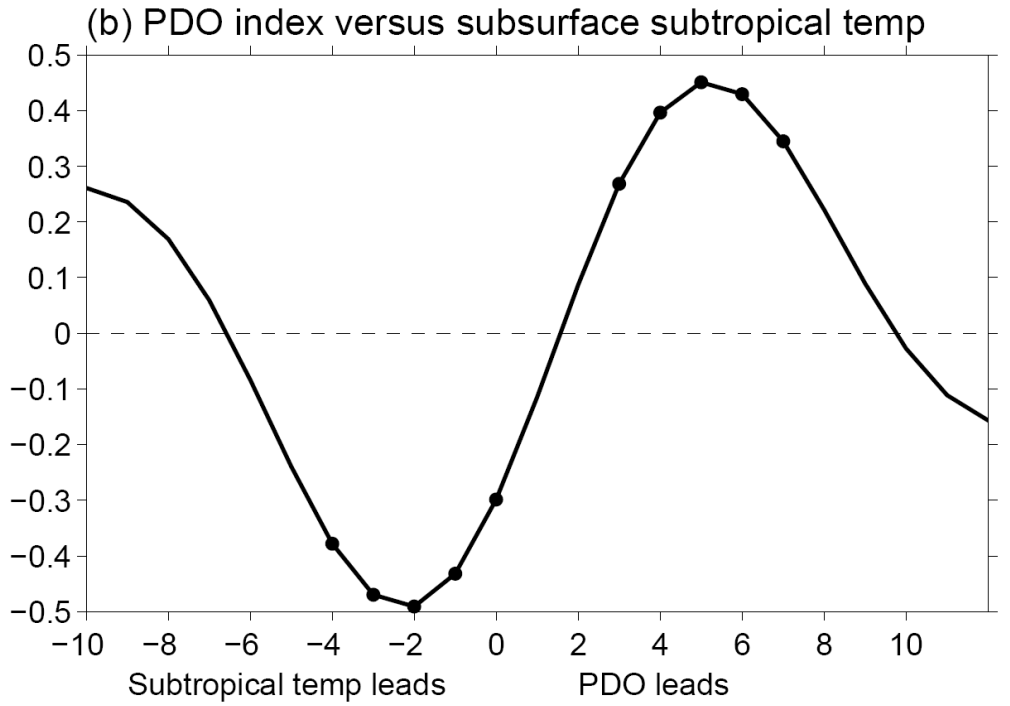

Figure 13: Lead-lag correlation between the annually (a) subsurface subpolar (48°-54°N, 160°-180°E, 150-350m) temperature and the PDO index in CM2.5_FLOR model. (b) Same as (a) but for the subsurface subtropical (25°-30°N, 140°-170°E, 100-300m) temperature. All data are 10-30-yr band-pass filtered before correlation. Positive (negative) values in x-axis indicate PDO leads (lags). The black point overlapped on the bold solid line denotes that the correlation is significant at 5% significance level based on the Monte-Carlo test.

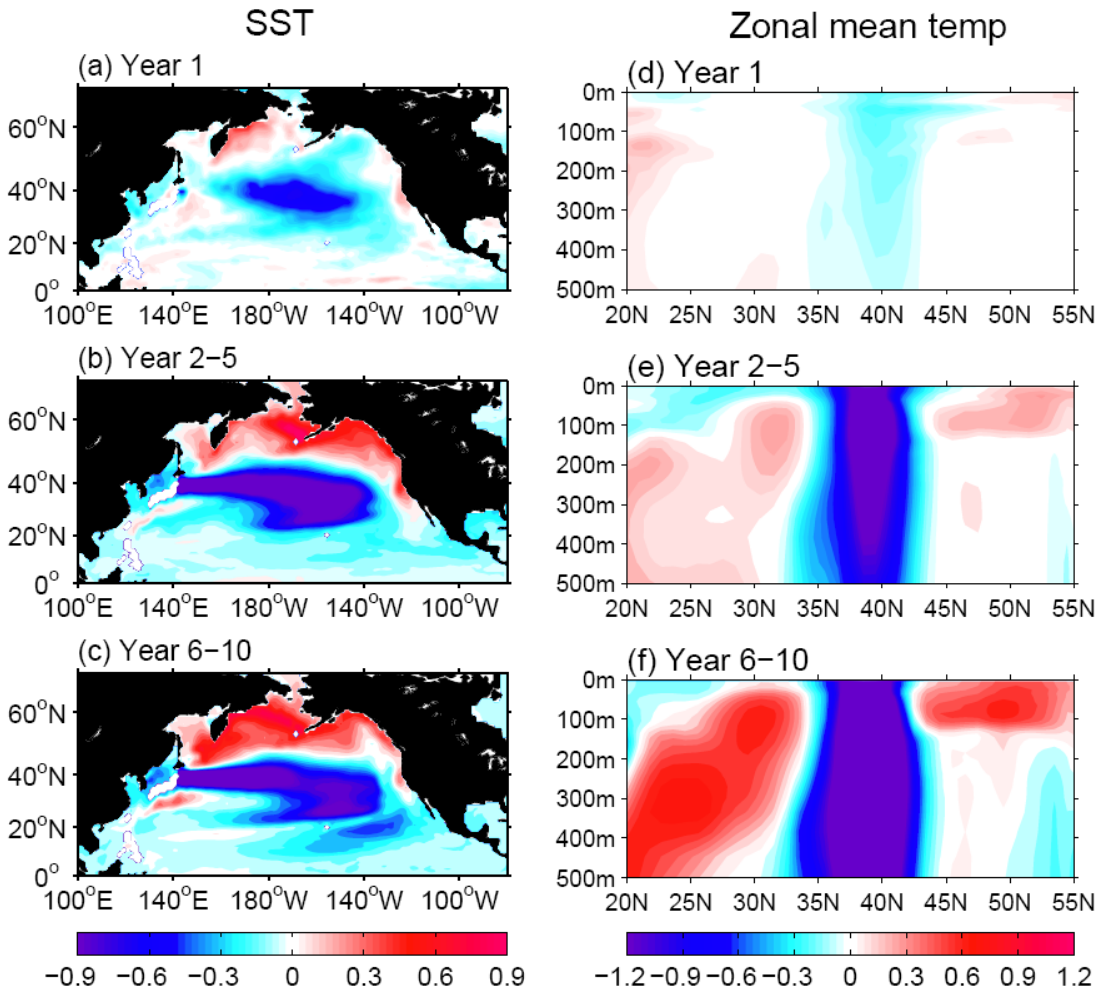

Figure 14: Time evolution of SST (left panel) and zonal mean (140°-180°E) temperature (right panel) anomalies in response to imposing a constant wind stress pattern corresponding to the PDO warm phase. Unit is °C.

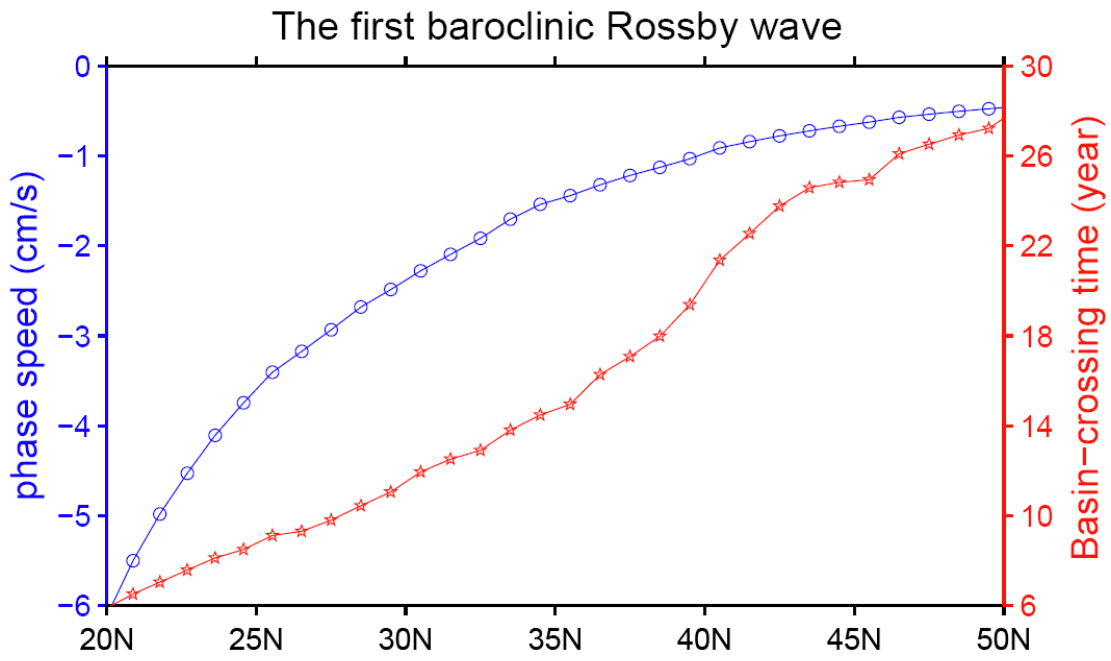

Figure 15: The averaged first baroclinic Rossby wave speed over the North Pacific Ocean (cm/s) and the corresponding basin-crossing time (year) in CM2.5_FLOR model.

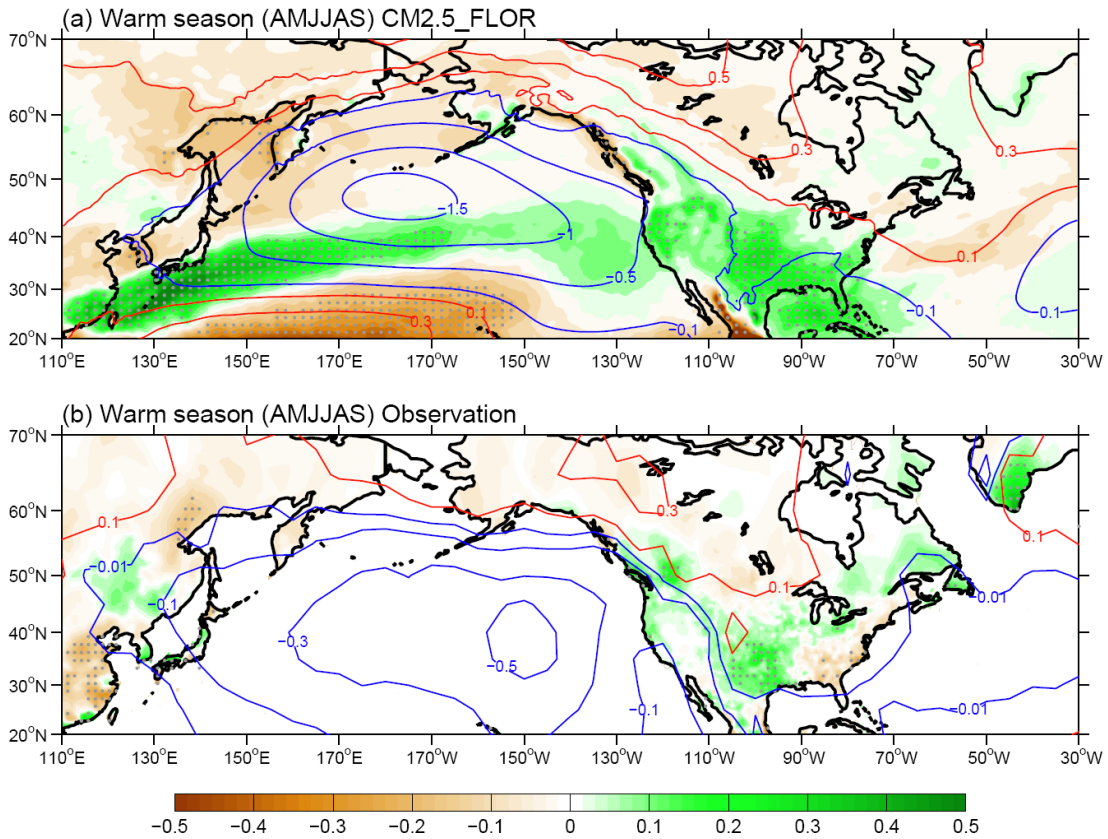

Figure 16: Regression of warm season (AMJJAS) precipitation (shading, Unit is mm/day) and sea level pressure (contours, Unit is hPa) against the normalized unfiltered PDO index in (a) CM2.5_FLOR model and (b) observation. The influence of ENSO is filtered out by using a linear regression onto the Niño3 index. The precipitation data is from Climatic Research Unit (CRU) high resolution (0.5×0.5 degree) precipitation time-series dataset and SLP data is from Met Office Hadley Center's sea level pressure HadSLP2.

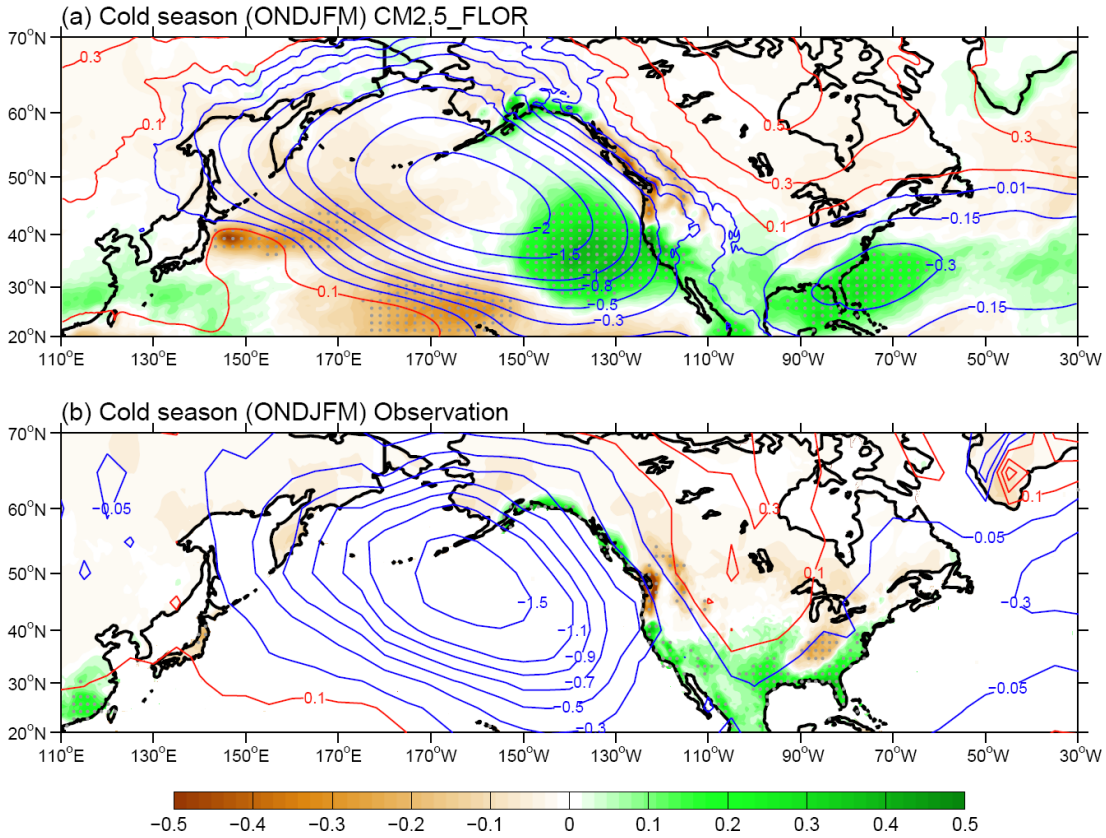

Figure 17: Same as Fig. 16 but for the cold season (ONDJFM).

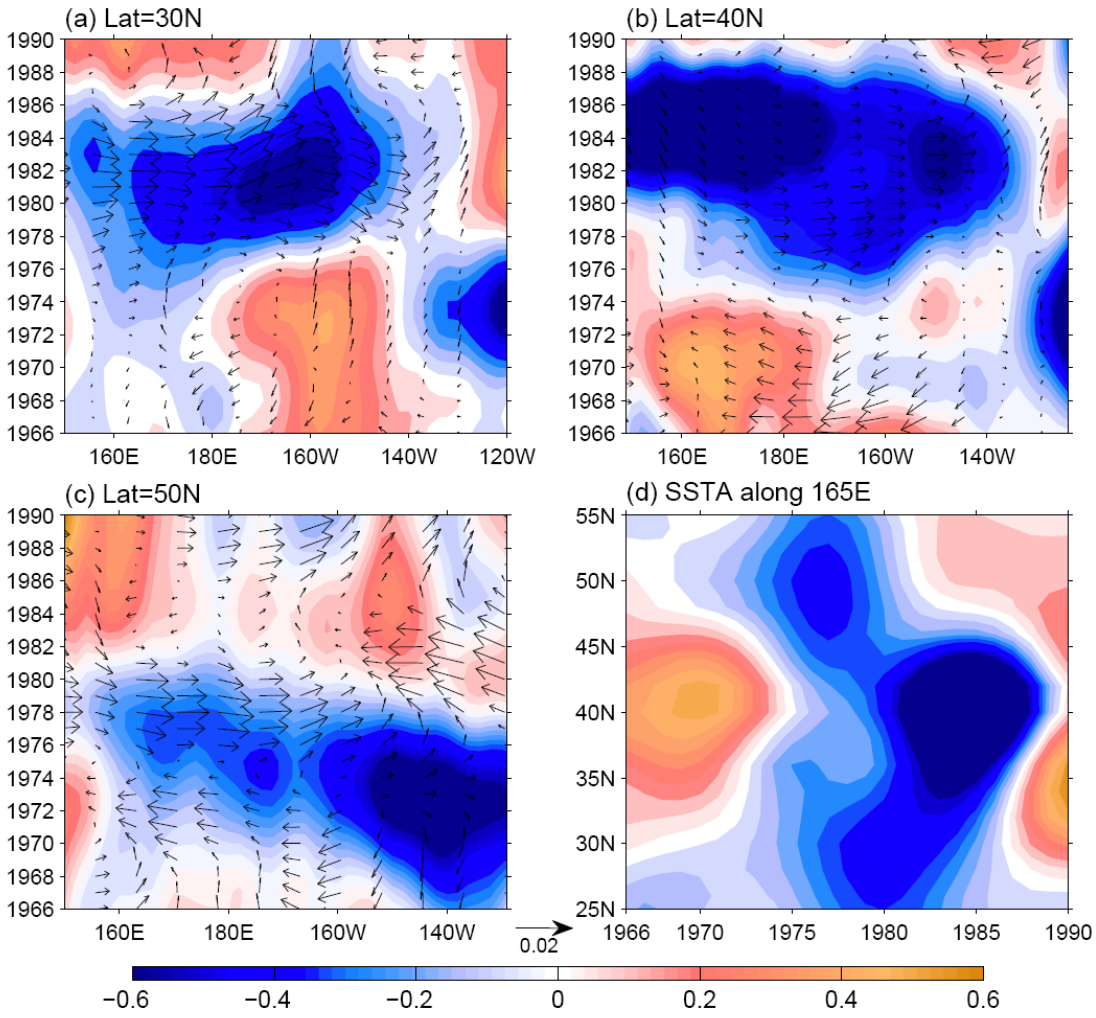

Figure 18: Shown are the 1976/1977 climate regime shifts over the North Pacific Ocean in observations. SST (shading, ^{o}C) and wind stress (vectors, N/m^2) anomalies along (a) 30^{o}N, (b) 40^{o}N and (c) 50^{o}N in the Pacific. (d) Hovmöller diagram of SST anomaly (^{o}C) evolution along 165^{o}E. All Data are 10-yr low pass filtered.